NASA/TP—2001–210801

NASA/TP-2001-210801
20010040758

Integrated Pulse Detonation Propulsion and Magnetohydrodynamic Power

R.J. Litchford
Marshall Space Flight Center, Marshall Space Flight Center, Alabama

January 2001

The NASA STI Program Office...in Profile

Since its founding, NASA has been dedicated to the advancement of aeronautics and space science. The NASA Scientific and Technical Information (STI) Program Office plays a key part in helping NASA maintain this important role.

The NASA STI Program Office is operated by Langley Research Center, the lead center for NASA's scientific and technical information. The NASA STI Program Office provides access to the NASA STI Database, the largest collection of aeronautical and space science STI in the world. The Program Office is also NASA's institutional mechanism for disseminating the results of its research and development activities. These results are published by NASA in the NASA STI Report Series, which includes the following report types:

- TECHNICAL PUBLICATION. Reports of completed research or a major significant phase of research that present the results of NASA programs and include extensive data or theoretical analysis. Includes compilations of significant scientific and technical data and information deemed to be of continuing reference value. NASA's counterpart of peer-reviewed formal professional papers but has less stringent limitations on manuscript length and extent of graphic presentations.

- TECHNICAL MEMORANDUM. Scientific and technical findings that are preliminary or of specialized interest, e.g., quick release reports, working papers, and bibliographies that contain minimal annotation. Does not contain extensive analysis.

- CONTRACTOR REPORT. Scientific and technical findings by NASA-sponsored contractors and grantees.

- CONFERENCE PUBLICATION. Collected papers from scientific and technical conferences, symposia, seminars, or other meetings sponsored or cosponsored by NASA.

- SPECIAL PUBLICATION. Scientific, technical, or historical information from NASA programs, projects, and mission, often concerned with subjects having substantial public interest.

- TECHNICAL TRANSLATION. English-language translations of foreign scientific and technical material pertinent to NASA's mission.

Specialized services that complement the STI Program Office's diverse offerings include creating custom thesauri, building customized databases, organizing and publishing research results...even providing videos.

For more information about the NASA STI Program Office, see the following:

- Access the NASA STI Program Home Page at ***http://www.sti.nasa.gov***

- E-mail your question via the Internet to help@sti.nasa.gov

- Fax your question to the NASA Access Help Desk at (301) 621–0134

- Telephone the NASA Access Help Desk at (301) 621–0390

- Write to:
  NASA Access Help Desk
  NASA Center for AeroSpace Information
  7121 Standard Drive
  Hanover, MD 21076–1320

NASA/TP—2001–210801

Integrated Pulse Detonation Propulsion and Magnetohydrodynamic Power

R.J. Litchford
Marshall Space Flight Center, Marshall Space Flight Center, Alabama

National Aeronautics and
Space Administration

Marshall Space Flight Center • MSFC, Alabama 35812

January 2001

Acknowledgments

The author of this work acknowledges the support of the Advanced Space Transportation Program (ASTP), a division of the Space Transportation Directorate, NASA George C. Marshall Space Flight Center. Results of the research reported herein were obtained at the request of ASTP's Space Transportation Research Project Office managed by John W. Cole. The NASA Principal Investigator was Ron J. Litchford, Chief Scientist, Space Transportation Research Project Office, TD15/ASTP. The author acknowledges contributive technical discussions with John T. Lineberry, President, LyTec LLC; Valentin A. Bityurin, Professor, Head of MHD Division/Coordinator of International Programs, Institute of High Temperatures (IVTAN), Russian Academy of Sciences, Moscow; Y.C.L. Susan Wu, President and CEO of ERC Incorporated; and Charles Merkle, Professor, University of Tennessee Space Institute.

This technical publication has been reviewed and is approved.

Garry M. Lyles
Program Manager
Advanced Space Transportation Program
TD15/ASTP
Marshall Space Flight Center

John W. Cole
Project Manager
Space Transportation Research
TD15/ASTP
Marshall Space Flight Center

Available from:

NASA Center for AeroSpace Information
7121 Standard Drive
Hanover, MD 21076–1320
(301) 621–0390

National Technical Information Service
5285 Port Royal Road
Springfield, VA 22161
(703) 487–4650

TABLE OF CONTENTS

LIST OF FIGURES

LIST OF FIGURES (Continued)

LIST OF TABLES

LIST OF ACRONYMS AND SYMBOLS

C_2H_2	acetylene
C_2H_4O	ethylene-oxide
C_2H_4	ethylene
C_2H_6	ethane
C_3H_6	propylene
C_3H_8	propane
C_6H_{14}	n-hexane
CH_4	methane
C-J	Chapman-Jouget
CsOH	cesium hydroxide
Cu	copper
cps	cycles per second
DDT	deflagration-to-detonation transition
emf	electromagnetic force
H_2	hydrogen
K_2CO_3	potassium carbonate
LRC	inductive-resistive-capacitive
MGOe	mega-Gauss Oersted
MHD	magnetohydrodynamic
O_2	oxygen
O/F	oxidizer-to-fuel (ratio)
PDE	pulse detonation engine
PDRE	pulse detonation rocket engine
TP	technical publication
W	tungsten

NOMENCLATURE

0	subscript denoting reference condition
A	area
A_c	chamber cross-sectional area
A_{eff}	effective cross-sectional area
A_{es}	area of equipotential surface
a	speed of sound
a_0	initial speed of sound
a_1	speed of sound before detonation
a_2	speed of sound after detonation
a_{CJ}	Chapman-Jouguet speed of sound
a_i	speed of sound in fresh mixture
B	magnetic flux density (magnetic induction)
B_{eff}	effective magnetic flux density
C	capacitance; engine flow coefficient
C_j	geometric parameter
C_p	constant pressure specific heat
c	chord of circle
D	detonation wave velocity
D_H	dimensionless detonation sensitivity parameter
d	tube diameter
d_c	critical diameter
E	electric field
E_a	activation energy
E_{app}	applied electric field
E_d	lump loss electric field
E_{eff}	effective electric field
E_{ind}	induced electric field
e	natural number (2.71828...)
e_s	scavenging efficiency
F	thrust
F_I	first phase thrust
F_{II}	second phase thrust

NOMENCLATURE (Continued)

f	fuel-to-air mass flow ratio; Lorentz body force
f_0	reference thrust level
g	Earth's gravitational acceleration
g_c	gravitational conversion factor
H	magnetic field
h	enthalpy; channel height
I	impulse
I_{sp}	fuel specific impulse
i	current
j	current density; index
j_{eff}	effective current density
K	load factor
L	length
L_c	chamber length
$\mathcal{L}$	inductance
M	Mach number
M_1	Mach number forward of detonation wave
M_2	Mach number rearward of detonation wave
m_p	mass of propellant
$\dot{m}$	mass flow rate
$\dot{m}'$	actual mass flow rate of fresh mixture
$\dot{m}_a$	mass flow rate of air
$\dot{m}_i$	scavenging mass flow rate
N	firing rate
n	number density
P	power
P_{avg}	average power
P_c	compressor power
P_p	push power
$\mathcal{P}$	power density
p	pressure
p_0	initial pressure
p_1	pressure before detonation
p_2	pressure after detonation

NOMENCLATURE (Continued)

p_{CJ}	Chapman-Jouguet pressure
p_e	exhaust pressure
p_i	scavenging pressure
p_p	pressure at piston surface
p_s	post-shock pressure
p_{wall}	pressure at wall
q	electric charge
q_f	fuel heating value
R	load resistance; gas constant
R_0	explosion length
R_1	gas constant before detonation
R_2	gas constant after detonation
R_d	lump loss resistance
R_h	magnetic force number
R_i	internal plasma resistance
R_m	magnetic Reynolds number
R_s	scavenging ratio
S	magnetic interaction parameter
T	temperature
T_0	initial temperature
T_1	temperature before detonation
T_2	temperature after detonation
T_{CJ}	Chapman-Jouguet temperature
T_i	scavenging temperature
T_s	post-shock temperature
t	time; electrode thickness
t_i	chemical induction time
t_{ig}	duration of energy release (igniter discharge time)
u	velocity
u_1	velocity forward of detonation wave
u_2	velocity rearward of detonation wave
u_{CJ}	Chapman-Jouguet particle velocity
u_b	burned gas velocity; gaseous slug velocity
u_p	velocity at piston surface

NOMENCLATURE (Continued)

u_s	post-shock velocity
V	terminal load voltage
V_c	chamber volume
V_{oc}	open circuit voltage
v	voltage; volume of fresh mixture
v_0	reference voltage
v_{app}	applied voltage
v_d	lump loss voltage
v_{dif}	differential voltage
v_s	scavenging volume
W	energy
W_D	electrical energy transfered per detonation
W_c	cylindrical detonation energy
W_j	source energy
W_p	planar detonation energy
W_s	spherical detonation energy
w	channel width; electron drift velocity
w_c	actual compression shaft work
w_{ca}	adiabatic compression shaft work
w_p	weight of propellant
x	coordinate axis
Y_c	pressure ratio function
y	coordinate axis
α	time rate of change in thrust
β	constant
Γ	trapping efficiency
γ	specific heat ratio
Δ	dimensionless voltage drop; induction length
δ	slug thickness
ε	electromotive force
ε_{eff}	effective electromotive force
ζ	radial distance from electrode surface

NOMENCLATURE (Continued)

η_c	compression efficiency
Λ	electric line source strength
λ	detonation cell size
ξ	efficiency coefficient; unity
π	natural number (3.14159...)
ρ	density
ρ_i	density of fresh mixture
ρ_s	scavenging density
σ	electrical conductivity
τ	characteristic time
τ_{I}	first phase characteristic time
τ_{II}	second phase characteristic time
ϕ	compressible flow function

TECHNICAL PUBLICATION

INTEGRATED PULSE DETONATION PROPULSION AND MAGNETOHYDRODYNAMIC POWER

1. INTRODUCTION

Contemporary interest in pulse detonation engines (PDE's) for various aerospace propulsion applications arises from the increased performance potential associated with unsteady flow effects and from anticipated cost reductions associated with a highly simplified design configuration. Unfortunately, the unsteady operational attributes of pulse detonation engines complicate their analysis when including nonideal effects, and it is difficult to make an accurate assessment of representative performance and cost benefits. Furthermore, design and optimization strategies are at an early stage of development, and there are critical operational issues, such as overall engine power requirements, that are in need of thoughtful attention. These uncertainties must be adequately addressed before the PDE will ever be realized in practice.

In general, PDE's can either collect air from the surrounding atmosphere to serve as the oxidizer or they can carry their oxidizer on board. In the former case, PDE's represent an attractive low-cost alternative to turbojets based on their potential for surpassing intrinsic limits on scalability, operating range, efficiency, and manufacturing costs. In the latter case, the device is referred to as a pulse detonation rocket engine (PDRE). The most common oxidizer for a PDRE is oxygen (O_2), which yields a combustible mixture that is easier to detonate than mixtures using air. Hydrogen (H_2) is probably the optimum fuel for PDRE's because of its ease of detonation and its high performance; however, hydrocarbon fuels are also of considerable practical interest.

PDE's produce thrust by intermittently detonating a charge of fuel and oxidizer placed inside a tube with one end closed and the other end open. The resulting propagation speed of the combustion detonation wave is extremely high, implying orders of magnitude increase in combustion rates relative to the deflagration mode. The detonation wave has the added benefit of attaining a higher peak pressure.

Indeed, the interest in PDE's arises primarily from advantages that accrue from the significant combustion pressure rise that is developed by the detonation process. Conventional rocket engines, for example, must obtain all of their compression from the turbopumps, whereas pulse detonation engines provide additional compression in the combustor. Thus, PDRE's are expected to achieve higher specific impulse (I_{sp}) than conventional rockets and require smaller turbopumps. The increase in I_{sp} and the decrease in turbopump capacity must be traded off against each other to determine the optimal engine choice. Similar arguments apply with respect to airbreathing applications.

A major objective of current development work is to demonstrate that PDE's can be operated at reduced levels of precompression such that flowpath turbomachinery can be greatly reduced. In this case, compression, combustion, and thrust-generating processes can be consolidated within a single component, yielding a high thrust-to-weight ratio, relative design simplicity, and enhanced reliability.

The scientific feasibility of the basic PDE concept has been proven in several experimental and theoretical studies, as noted in recently published review articles.[1,2] Significant strides are also being made with respect to the development of design strategies and performance optimization.[3] However, there are certain developmental issues affecting the application of pulse detonation propulsion systems which have yet to be fully resolved.

Practical detonative combustion engines, for example, require a repetitive cycle of charge induction, mixing, initiation/propagation of the detonation wave, and expulsion/scavenging of the combustion product gases. Clearly, the performance and power density of such a device depends upon the maximum rate at which this cycle can be successfully implemented. The key point here being that accomplishment of these tasks requires power that must be supplied by either the engine or delivered from an auxiliary source.

For instance, the energy needed for direct detonation initiation may be considerable, depending upon the specific fuel-oxidizer combination, and the pumping power required for effective scavenging of the chamber is a critical design consideration. PDE's, however, have no shaft power; therefore, an external power source or utilization of an alternative energy conversion scheme must be relied on. As such, this research investigates the opportunity for direct electric power production using the detonation combustion wave to drive a magnetohydrodynamic (MHD) generator integrated into the engine design.

The author is aware, of course, that a detonation-driven MHD generator can only convert the kinetic energy of the combustion products into electrical power. Thus, the enthalpy extraction efficiency of such a device will not be comparable with a typical generator configuration utilizing thermal combustion conditions and a flow-accelerating nozzle. Nevertheless, the detonation-driven MHD generator may, despite its intrinsic efficiency limitations, prove effective for specialized airborne missions.

A review of the open literature revealed only one paper directly addressing this concept on an experimental basis, and it was published by researchers from the Krzhizanovsky Power Institute in Moscow.[4] Their motive at the time was the development of peak/emergency power stations which would operate on natural gas. Because detonation-driven MHD power avoids the need for a high-temperature heat exchanger, a large compressor station, and a complex dc-to-ac conversion system, they realized that the intrinsic energy conversion inefficiencies associated with this device could be offset by the extremely low capital costs of construction.

These researchers used a natural gas/O_2-fired detonation tube seeded with a potassium carbonate (K_2CO_3) aqueous solution to drive a 16-mm-diameter linear MHD channel subjected to a 0.23 T magnetic induction and were able to extract electrical power while running the system at repetition rates approaching 100 cps for a duration of 2 hr. The channel electrodes were segmented, but the active MHD length was not specified. Observed cycle-to-cycle variations in detonation velocity did not exceed 1.5 percent, and the wall heat flux accounted for 25 percent of the released combustion energy. The power output peaked at $\approx$0.1 W_e at a load impedance near 10 Ω. The maximum effective electrical conductivity measured during

these tests was $\langle\sigma\rangle$ = 3.3 S/m. These test results validated the fundamental technical feasibility of pulse detonation-driven MHD power and provided confidence that the concept could be extended for application to aerospace propulsion systems.

The fundamental objective of this line of research was to address developmental concerns which affect the prospects for realizing an integrated pulse detonation propulsion and MHD power system. In this technical publication (TP), the energy requirements for direct detonation initiation of various fuel-oxidizer mixtures as well as the pumping power requirements necessary for effective scavenging of the chamber are critically examined. In addition, this TP reports a series of experiments designed to investigate the basic engineering performance characteristics of a laboratory-scale pulse-detonation-driven MHD generator. This included quantification of ionization properties behind the detonation wave and evaluation of electrical power extraction characteristics from a short-length, continuous-electrode Faraday channel. A simple electrodynamic model incorporating near-electrode potential losses is developed and is used to correlate the experimental work and to extrapolate performance at increased scales. The experimental results reported here are only for stoichiometric mixtures of acetylene (C_2H_2) and O_2 with an atomized spray of cesium hydroxide (CsOH) dissolved in alcohol as an ionization seed in the active MHD region. As part of the experimental work, an engine stand was developed which allowed direct time-resolved measurements of system thrust both with and without MHD interaction.

2. OPERATIONAL POWER REQUIREMENTS

The power required to operate a PDE is dominated by the electrical power consumed in the detonation initiation process and by the power needed to transport the propellants. Without loss of generality, assume that the pumping power can be delivered using an electric drive. The anticipated power consumption requirements for these operational functions are now examined.

2.1 Direct Detonation Initiation

Detonation initiation may be accomplished through one of two possible modes: (1) A slow deflagration-to-detonation transition (DDT) via an accelerating combustion wave and (2) a fast, direct initiation process in which the blast wave from a strong igniter produces the immediate onset of detonation. Because the flame travel necessary for DDT transition is on the order of 1 m for the most sensitive fuels available, the slow DDT mode does not appear promising for PDE applications. Inquiry is therefore confined to the direct initiation mode in which the major parameter of interest is the critical igniter energy. A thorough and complete discussion with respect to both modes of detonation initiation may be found in the survey paper of Lee.[5]

The most common semiempirical methods for determining the critical detonation energy are based on the linear detonation tube method first proposed by Zeldovich et al. in which a spherical detonation is initiated by firing a planar detonation wave from a linear tube into a larger volume.[6] Experimentally, it is found that the planar wave will transform into a spherical detonation wave if the tube diameter d exceeds a certain critical value d_c (i.e., $d > d_c$). If $d < d_c$, the reaction zone will decouple from the shock, and a spherical deflagration wave results.

The critical tube diameter is known as a dynamic parameter of detonation in that it is governed by both the chemical reaction rates and the three-dimensional structure of the detonation wave and cannot be determined from the equilibrium (static) Chapman-Jouget (C-J) theory.[7] Other dynamic parameters include the cell size λ, the initiation energy W_s, the chemical induction time t_i, the induction length $\Delta = ut_i$ (where u is the particle velocity relative to the shock), and the detonation limits. It turns out that an extensive array of experimental evidence indicates a universal linear relationship between d_c and λ; that is, $d_c = 13\,\lambda$. This universal correlation is extremely useful in practice when available experimental apparatus permit the direct determination of one parameter rather than the other.

Once λ or d_c has been experimentally determined, a number of semiempirical point blast initiation models have been developed which can be used to estimate the critical initiation energy W_s for an unconfined spherical detonation wave. Some of these models are described and compared against experimental data in the work of Benedick et al.[8] A particularly simple but useful correlation is the "work done" model of Lee and Matsui.[9] This model assumes that as the wave emerges from the tube, the energy is delivered to the outside volume via the work done by the interface that separates the expanding combustion products from the unreacted mixture. A simple expression is thus obtained relating W_s to both d_c and the C-J states of the mixture:

$$W_s = \frac{\pi p_{CJ} u_{CJ} d_c^3}{24 a_{CJ}} \quad , \tag{1}$$

where p_{CJ} is the C-J detonation pressure, u_{CJ} is the C-J particle velocity, and a_{CJ} is the speed of sound behind the C-J detonation.

It is also common practice to represent the critical initiation energy in terms of a dimensionless number D_H formed by the ratio of the critical initiation energy of the fuel-oxidizer mixture of interest to that of C_2H_2/O_2. Thus, D_H represents a relative measure of detonation sensitivity.

Another extremely useful parameter is the explosion length R_0 associated with a given source energy:

$$R_0 = \left(\frac{W_j}{p_0} \right)^{1/(j+1)} \quad , \tag{2}$$

where $j = 0, 1, 2$ for planar, cylindrical, and spherical geometries, respectively; W_j is the source energy per unit area, per unit length, or just the energy for the three geometries; and p_0 is the initial gas pressure. The importance of R_0 is derived from the fact that it is equivalent for all three geometries.[5] Thus, once the critical initiation energy is known for the spherical detonation, it is possible to obtain the initiation energy for the planar (W_p) and cylindrical (W_c) geometries through the following scaling relationship:

$$R_0 = \frac{W_s}{W_c} = \frac{W_c}{W_p} \quad . \tag{3}$$

Table 1 represents the dynamic detonation parameters for a broad range of fuel-oxidizer mixtures as deduced through the application of the "work done" model and through the explosion length scaling relationship to the experimental data of Matsui and Lee[10] and Beeson et al.[11] These data correspond to near stoichiometric compositions at 1 atm pressure.

It is evident from these results that the detonation initiation energy required for H_2/O_2 mixtures is roughly 10^3 times greater than that for C_2H_2/O_2 mixtures. This is a minimal requirement and can easily be achieved with an auxiliary onboard power supply. For an H_2/air mixture, however, the detonation initiation energy requirement becomes several orders of magnitude higher and the use of auxiliary onboard power becomes more problematic. Note that the results for an n-hexane/air mixture may be taken as representative of a jet fuel/air mixture and that the electrical power demand for detonation initiation in this case will also be significant. In general, the conclusion reached is that the use of practical fuel-oxidizer mixtures in high firing rate PDE's will require a substantial amount of electrical power for direct detonation initiation. This power demand can be minimized by using an initiator tube of the smallest feasible diameter (as defined by d_c), but it is evident that an integrated power generation system would prove advantageous.

Table 1. Dynamic detonation parameters at near stoichiometric composition.

Mixture	d_c (cm)	λ (mm)	D_H	W_s (J)	R_0 (m)	W_p (J/cm^2)
Acetylene/Oxygen (C_2H_2/O_2)	0.158	0.122	1	3.83×10^{-4}	1.56×10^{-3}	1.57×10^{-2}
Ethylene-Oxide/Oxygen (C_2H_4O/O_2)	0.3	0.231	3.1×10^{1}	1.2×10^{-2}	4.91×10^{-3}	4.98×10^{-2}
Ethylene/Oxygen (C_2H_4/O_2)	0.647	0.498	1.9×10^{2}	7.2×10^{-2}	8.92×10^{-3}	9.05×10^{-2}
Propylene/Oxygen (C_3H_6/O_2)	0.841	0.647	5.3×10^{2}	2.03×10^{-1}	1.26×10^{-2}	1.28×10^{-1}
Propane/Oxygen (C_3H_8/O_2)	1.01	0.777	1.5×10^{3}	5.77×10^{-1}	1.78×10^{-2}	1.82×10^{-1}
Ethane/Oxygen (C_2H_6/O_2)	1.1	0.846	2.8×10^{3}	1.07	2.19×10^{-2}	2.23×10^{-1}
Methane/Oxygen (CH_4/O_2)	5.28	4.06	1.3×10^{5}	5.07×10^{-1}	7.94×10	8.04×10^{-1}
Hydrogen/Oxygen (H_2/O_2)	1.99	1.53	4.1×10^{3}	1.58	2.5×10^{-2}	2.53×10^{-1}
Acetylene/Air (C_2H_2/Air)	8.1	6.23	3.4×10^{5}	1.29×10^{2}	0.108	1.11
Ethylene-Oxide/Air (C_2H_4O/Air)	30	23.1	2×10^{7}	7.62×10^{3}	0.422	4.28
Ethylene/Air (C_2H_4/Air)	80	61.5	3.1×10^{8}	1.2×10^{5}	1.06	10.7
n-Hexane/Air (C_6H_{14}/Air)	144	111	1.8×10^{9}	7×10^{5}	1.9	19.4
Propylene/Air (C_3H_6/Air)	150	115	2×10^{9}	7.55×10^{5}	1.95	19.8
Propane/Air (C_3H_8/Air)	220	169	6.6×10^{8}	2.52×10^{6}	2.92	29.6
Ethane/Air (C_2H_6/Air)	280	215	1.3×10^{10}	5.09×10^{6}	3.69	37.4
Methane/Air (CH_4/Air)	1,020	785	5.9×10^{11}	2.28×10^{8}	13.1	133
Hydrogen/Air (H_2/Air)	196	151	1.1×10^{10}	4.16×10^{6}	3.45	35

*All parameters deduced from experimental data of Matsui and Lee[10] and Beeson et al.[11]

The critical energy of detonation is also dependent upon the rate at which energy is deposited by the igniter (i.e., igniter power). In general, the critical energy decreases with a decrease in the duration of energy release t_{ig} (i.e., as igniter power increases). This behavior has important implications with respect to the optimal design of an igniter circuit for a PDE.

A simple theoretical model for determining the correlation between critical energy and power required for direct initiation has been formulated by Abouseif and Toong.[12] This model considers the flow generated by the motion of a constant velocity shock wave in planar, cylindrical, and spherical geometries. The shock increases the temperature and pressure of the detonable mixture, and ignition can occur in the shock-heated gas after a period corresponding to the induction time. If this blast wave is sufficiently strong, the reaction zone is able to couple with the shock wave to form a detonation wave.

The basis for the model is the observation that a constant velocity shock can be generated by a constant velocity piston in the three geometries of interest.[13] Furthermore, Chu demonstrated that such a constant velocity piston could be realized in practice by means of an appropriate energy deposition rate.[14] Abousief and Toong took this source power relationship for generating a constant velocity piston motion and hypothesized that the chemical induction time for detonation is equivalent to the duration of piston motion for initiating detonation. This hypothesis was verified for the planar case through numerical calculations. Following this hypothesis, the necessary power P of the energy source is obtained from Chu's relationship in the form

$$P = \frac{\gamma}{\gamma - 1} C_j p_p u_p^{j+1} t_i^j \quad , \tag{4}$$

where $C_j = 1, 2\pi, 4\pi$ for $j = 0, 1, 2$ for the three geometries, respectively; p_p and u_p are the pressure and velocity at the piston surface, γ is the ratio of specific heats, and t_i is the induction time. The total deposited energy is obtained by integrating the power relationship over the induction time and it follows that

$$W_c = \frac{\gamma}{\gamma - 1} \frac{C_j}{j+1} p_p u_p^{j+1} t_i^{j+1} \quad . \tag{5}$$

The critical energy is time dependent for the cylindrical and spherical geometries. In order to relate the critical source energy to a critical source power, it is useful to define an average or effective power as

$$P_{av} = \frac{W_c}{t_i} = \frac{\gamma}{\gamma - 1} \frac{C_j}{j+1} p_p u_p^{j+1} t_i^j \quad . \tag{6}$$

Determination of the pressure and velocity of the piston is simple for the planar geometry. In this case, the entire flow field bound by the piston and the shock wave is uniform and identical to that just downstream of the shock. Thus, p_p and u_p are equivalent to the conditions just downstream of the shock front (i.e., p_s and u_s as given by the Rankine-Hugoniot relations for a given blast wave strength of Mach number M):[15]

$$\frac{p_s}{p_0} = \frac{2\gamma M^2 + 1 - \gamma}{\gamma + 1} \tag{7}$$

$$\frac{T_s}{T_0} = \frac{[2\gamma M^2 + 1 - \gamma][(\gamma - 1)M^2 + 2]}{(\gamma + 1)^2 M^2} \tag{8}$$

$$\frac{u_s}{a_0} = M\left[1 - \frac{(\gamma - 1)M^2 + 2}{(\gamma + 1)M^2}\right] . \tag{9}$$

Note that specification of the shock Mach number yields a post-shock temperature T_s that can be used to deduce t_i.

For a one-step, first-order Arrhenius rate expression, the chemical induction time is proportional to an exponential function involving the activation energy E_a and the temperature T_s:

$$t_i \propto \exp\left[\frac{E_a}{RT_s}\right] . \tag{10}$$

For estimation purposes, a ratio is formed between the induction time for any blast wave strength to the induction time $t_{i,CJ}$ for a C-J wave such that

$$t_i = t_{i,CJ} \exp\left[\frac{E_a}{R}\left(\frac{1}{T_s} - \frac{1}{T_{CJ}}\right)\right] , \tag{11}$$

where T_{CJ} is the temperature behind a C-J shock wave.

This methodology is demonstrated for stochiometric H_2/O_2 and H_2/air mixtures since they are of great practical interest. The activation energy for H_2/air is taken as E_a = 16.5 kcal/mol, as suggested by Shepherd.[16] The activation energy for H_2/air mixtures was taken as E_a = 32 kcal/mol, as deduced by Moen et al.[17] The C-J induction times are estimated by fitting available kinetic data. The results of these fits are shown in figure 1 where $t_{i,CJ} \approx 8.8 \times 10^{-8}$ sec for H_2/O_2 and $t_{i,CJ} \approx 2.5 \times 10^{-5}$ sec for H_2/air.

Predictions for the critical initiation energy as a function of average deposition power are shown in figure 2 for a planar geometry. As anticipated, the blast wave strength is seen to increase with power input and the critical initiation energy asymptotically approaches a minimum threshold value. It is again clear that the electrical power requirements for H_2/air mixtures can be more than 10 times greater than for H_2/O_2 mixtures.

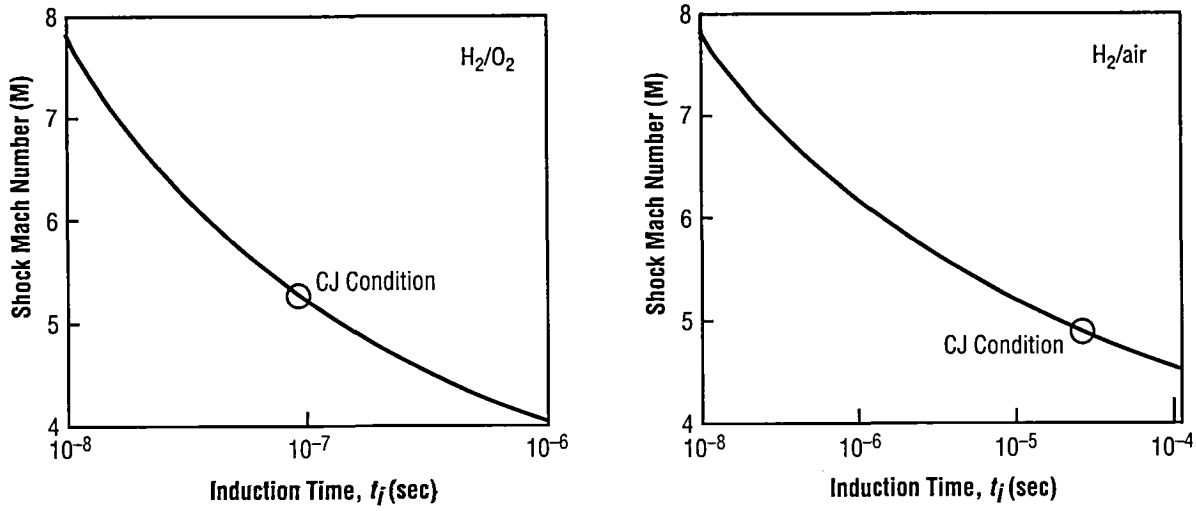

Figure 1. Variation of chemical induction time with blast wave strength for stoichiometric H_2/O_2 and H_2/air mixtures. Based on empirical fit of C-J induction time to available kinetic data.

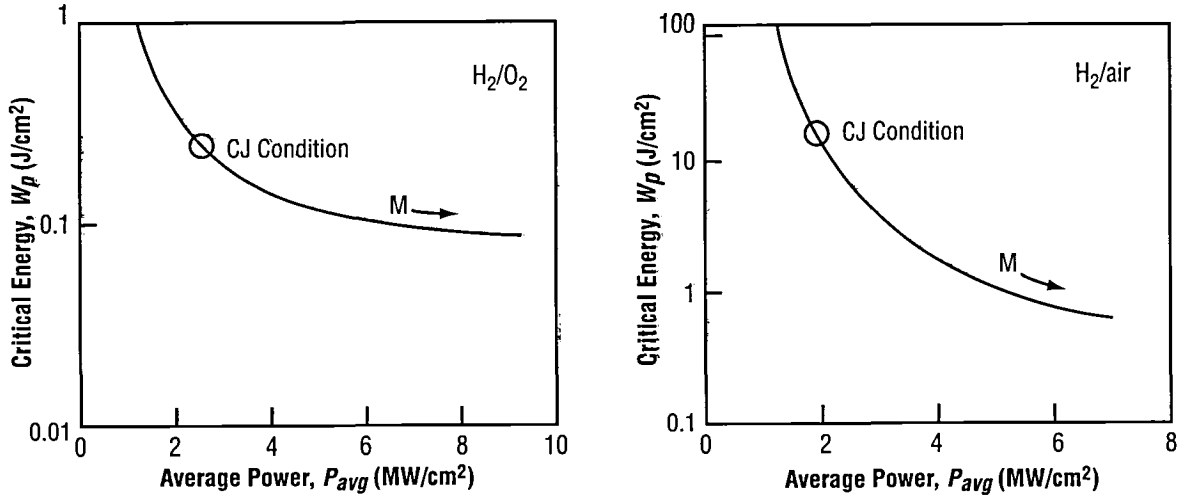

Figure 2. Predicted critical initiation energy versus average deposition power for planar detonations in stoichiometric H_2/O_2 and H_2/air mixtures.

2.2 Chamber Scavenging

A distinguishing feature of PDE's is that the blowdown of gas from the chamber during every pulse is coupled with a scavenging and recharging process. Such operation is possible only when a propellant-pumping mechanism is available. In general, the cylinder pressure will briefly fall below the exhaust pressure p_e after the blowdown process due to the inertia of the exhaust gases. Once the inlet valve is open, fresh mixture will begin to flow into the chamber as soon as the chamber pressure falls below the scavenging pressure p_i. This inflow of fresh mixture continues as long as the inlet valve remains open and the inlet total pressure exceeds the pressure in the chamber.

It has been suggested that a favorable scavenging effect may be obtained through proper tuning of the pressure waves in the exhaust and inlet sections of the engine. That is, the chamber vacuum pulled by the blowdown process may be strong enough to eliminate the need for a scavenging compressor such that self-aspirating operation becomes feasible. However, it seems unlikely that a design strategy of this type can be implemented over a wide range of operating conditions. In all probability, some pumping power will be required to achieve effective scavenging and recharging.

In an ideal scavenging process, the fresh mixture would push the residual chamber gases out of the tube without mixing or exchanging heat. This process would continue until the fresh mixture just fills the chamber without escaping through the exhaust. In an actual engine, of course, some mixing and heat exchange would occur and some of the fresh mixture would be lost through the exhaust. Furthermore, a nonreactive buffer gas layer would probably be required between the fresh mixture and residual gases in order to prevent preignition. This would represent even further degradation of the scavenging process.

The effectiveness of the actual scavenging process with respect to the ideal process can be expressed in terms of some predefined parameters. For example, the fresh mixture supplied in the ideal scavenging process would be that which would just fill the chamber at inlet temperature and exhaust pressure (i.e., $NV_c\rho_s$ where N is the firing rate, V_c is the chamber volume, and $\rho_s = \rho_s(T_i,p_e)$.

Thus, a scavenging ratio R_s may be defined as the ratio of the actual mass supplied to the ideal mass supplied:

$$R_s = \frac{\dot{m}_a}{NV_c\rho_s} \quad . \tag{12}$$

A scavenging efficiency e_s may also be defined as the ratio of the actual mass of fresh mixture retained in the chamber to that for an ideal scavenging process:

$$e_s = \frac{\dot{m}'_a}{NV_c\rho_s} \quad . \tag{13}$$

These two parameters may be related to each other through the introduction of a trapping efficiency Γ:

$$e_s = \Gamma R_s \quad . \tag{14}$$

It is useful at this point to consider an extreme case where the fresh mixture mixes completely with the residual gases under the assumption that the residual gases have the same temperature and molecular weight as the fresh mixture. For this perfect mixing model, mass conservation may be expressed in the following differential form:

$$dv - e_s dv = V_c de_s \quad , \tag{15}$$

where v is the volume of fresh mixture which has flowed into the chamber up to a given instant in time. Separating variables and integrating over the scavenging period yields

$$\ln(1-e_s) = \frac{-v_s}{V_c} \quad . \tag{16}$$

But $R_s = v_s/V_c$ by definition and the following working relationship is obtained:

$$e_s = 1 - e^{-R_s} \quad . \tag{17}$$

Substituting equation (14) yields an additional expression for the variation in trapping efficiency with scavenging ratio for the perfect mixing model

$$\Gamma = \frac{1-e^{-R_s}}{R_s} \quad . \tag{18}$$

Figure 3 shows the variation in e_s and Γ with R_s for the perfect mixing model. For an ideal scavenging process, $\Gamma = 1$ and $e_s = R_s$. In practice, e_s and R_s could be measured and used as a quantitative measure of the scavenging effectiveness associated with a particular engine design.

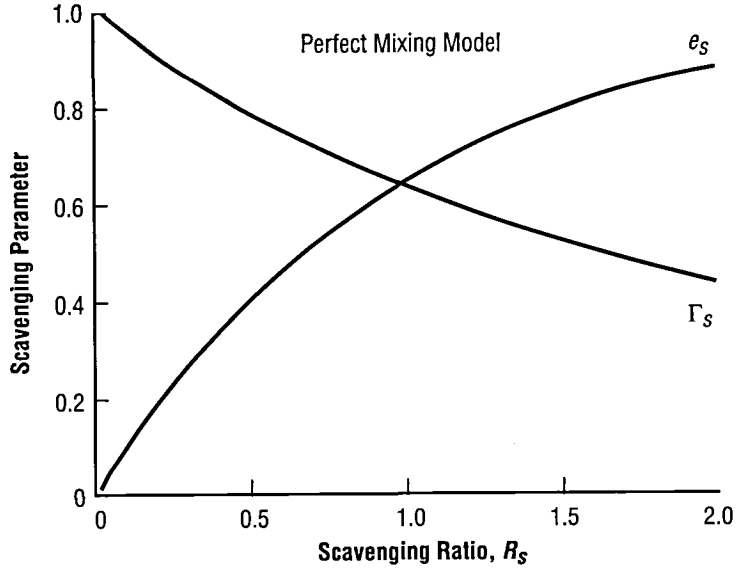

Figure 3. Variation in scavenging efficiency e_s and trapping efficiency Γ with scavenging ratio R_s for a perfect mixing model.

Although the scavenging efficiency and scavenging ratio are highly important characteristics of a PDE, the power required to attain a given scavenging ratio is of equal or greater interest. For the purpose of analysis, consider the flow train sketched in figure 4 as an effective representation of an actual engine.

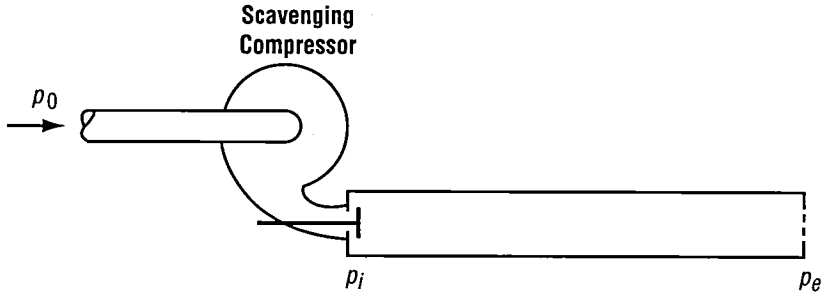

Figure 4. Schematic representation of PDE flow train.

First note that the power to scavenge is a function of the mass flow of fresh charge and the pressure at which this charge must be delivered to the inlet port of the chamber. The mass flow is given by

$$\dot{m}_a = A_c C a_i \rho_i \phi \quad , \tag{19}$$

where A_c is the chamber cross-sectional area (i.e., the characteristic cross-sectional area), C is the engine flow coefficient, a_i is the speed of sound in the fresh mixture, and ϕ is the compressible flow function:

$$\phi = \sqrt{\frac{2}{\gamma - 1}\left[\left(\frac{p_e}{p_i}\right)^{\frac{2}{\gamma}} - \left(\frac{p_e}{p_i}\right)^{\frac{\gamma+1}{\gamma}}\right]} \quad . \tag{20}$$

By substituting equation (19) into equation (12), one obtains the expression

$$R_s = \left(\frac{Ca_i}{NL_c}\right)\left(\frac{\rho_i}{\rho_s}\right)\phi \quad , \tag{21}$$

where L_c is the chamber length. It is now possible to replace ρ_i/ρ_s with p_i/p_e since both densities are evaluated at the inlet temperature. The result is a relationship for the pressure ratio required for scavenging as a function of characteristic engine parameters:

$$\frac{p_i}{p_e} = \frac{R_s N L_c}{C a_i}\frac{1}{\phi} \quad . \tag{22}$$

Figure 5 shows the variation in scavenging pressure as a function of a characteristic engine velocity assuming air as a working fluid. Note that the pressure differential required for effective scavenging can become significantly large under some circumstances, implying the need for high pumping power.

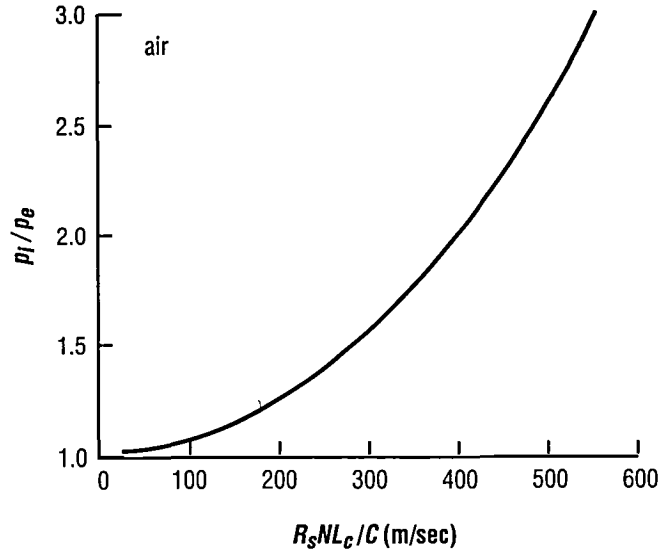

Figure 5. Variation in scavenging pressure ratio as a function of characteristic engine velocity. Assumes air as the working fluid.

For a given required scavenging pressure p_i and inlet pressure p_0, it is possible to estimate the necessary pumping power. For adiabatic, isentropic compression of an ideal gas, the shaft work w_{ca} may be expressed as

$$w_{ca} = C_{p0} T_0 Y_c \quad , \tag{23}$$

where C_{p0} is the constant pressure specific heat and Y_c is a pressure ratio function for the compressor:

$$Y_c = \left(\frac{p_i}{p_0} \right)^{\frac{\gamma-1}{\gamma}} - 1 \quad . \tag{24}$$

Therefore, the power required for adiabatic, isentropic compression of an idea gas is given by

$$P_{ca} = \dot{m}_i w_{ca} = \dot{m}_i C_{p0} T_0 Y_c \quad . \tag{25}$$

The actual shaft work w_c may be expressed as

$$w_c = C_{p0} \left(T_i - T_0 \right) \quad , \tag{26}$$

and the actual power required for compression is given by

$$P_c = \dot{m}_i w_c = \dot{m}_i C_{p0} \left(T_i - T_0 \right) \quad . \tag{27}$$

At this point it is beneficial to define a compression efficiency as the ratio of the adiabatic shaft power to the actual shaft power:

$$\eta_c = \frac{P_{ca}}{P_c} = \frac{T_0 Y_c}{T_i - T_0} \quad , \tag{28}$$

such that

$$P_c = \frac{P_{ca}}{\eta_c} = \frac{\dot{m}_i C_{p0} T_0 Y_c}{\eta_c} \tag{29}$$

and

$$\frac{T_i}{T_0} = \left(1 + \frac{Y_c}{\eta_c}\right) \quad . \tag{30}$$

An energy density parameter may now be formed by substituting equation (12) into equation (29):

$$\frac{P_c}{N \rho_s V_c R_s} = \frac{C_{p0} T_0 Y_c}{\eta_c} \quad . \tag{31}$$

Figure 6 shows the pumping power per unit mass flow as a function of the scavenging pressure ratio p_i/p_0, assuming air as the working fluid with $\eta_c = 0.9$. Note that equation (31) is a useful scaling relation in terms of scavenging parameters and demonstrates the level of pumping power that might be required in a practical engine.

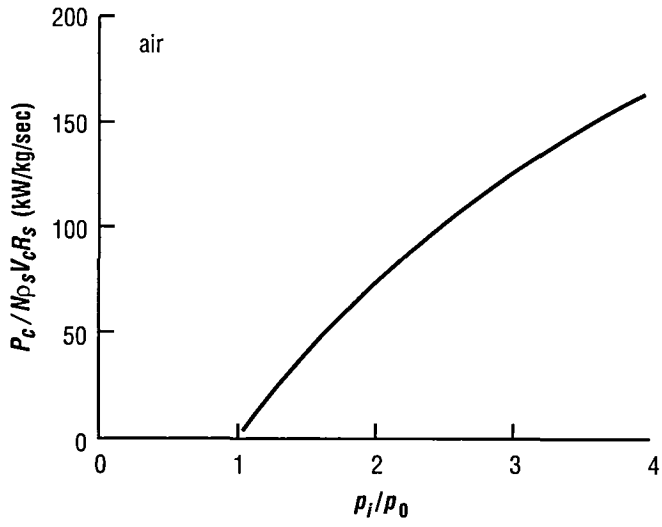

Figure 6. Variation in pumping power per unit mass flow as a function of the scavenging pressure ratio. Assumes air as working fluid with $\eta_c = 0.9$.

3. THEORETICAL AND EXPERIMENTAL PERFORMANCE

3.1 Experimental Apparatus

The general experimental arrangement is shown schematically in figure 7. The laboratory-scale detonation tube is closed at one end and various plasma diagnostic and MHD channels can be attached to the open end using an area transition adapter. A permanent magnet assembly and an electromagnet were custom fabricated for establishing MHD interaction in the channel. All of the experiments were conducted in a single-shot mode where the system is evacuated, charged to atmospheric pressure with premixed combustibles, and ultimately detonated using a high-voltage spark discharge near the closed end of the tube. During this process, a thin membrane separates the chamber volume from the surrounding atmosphere until it is ruptured by the detonation wave. Ionization seed is introduced using an atomizing injector that is located near the open end of the detonation tube and oriented in such a way as to direct the seed spray along the length of the attached channel. The entire tube/channel assembly is suspended on rollers and preloaded against a piezoelectric-type dynamic load cell. Dynamic pressure transducers were installed in the tube to measure detonation wave strength and to provide time-of-flight measurement of detonation wave speed. The design/configuration of the individual components making up the experimental apparatus are discussed in detail in the following subsections.

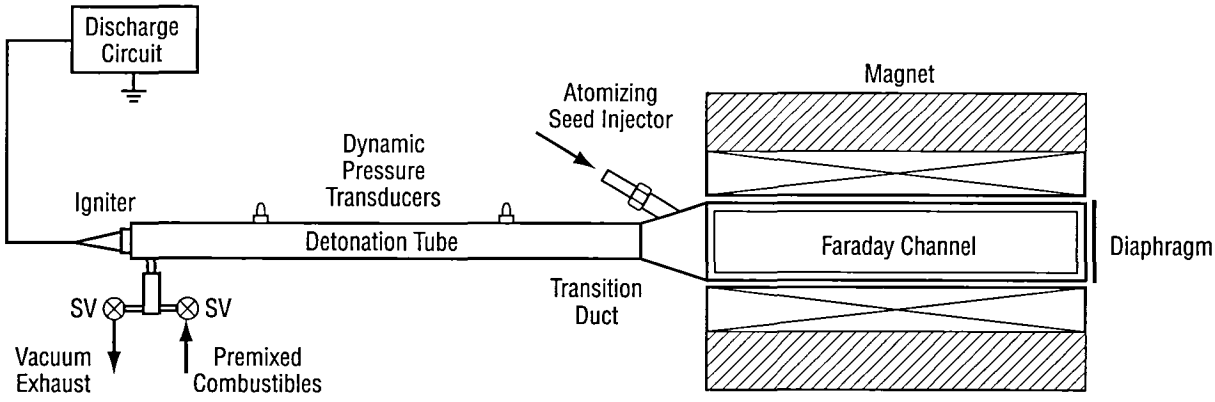

Figure 7. General schematic of laboratory-scale pulse detonation MHD apparatus.

3.1.1 Detonation Tube

The detonation tube is constructed from a 1-m-long section of schedule-40 steel pipe having a nominal inside diameter of 2.54 cm. The detailed configuration of this tube is shown in figure 8. The head of the detonation tube is sealed with a pipe cap in which fitting connectors have been installed for evacuating the tube and introducing premixed combustibles. The open end is flanged for attachment of an area transition adapter and diagnostic/MHD channels.

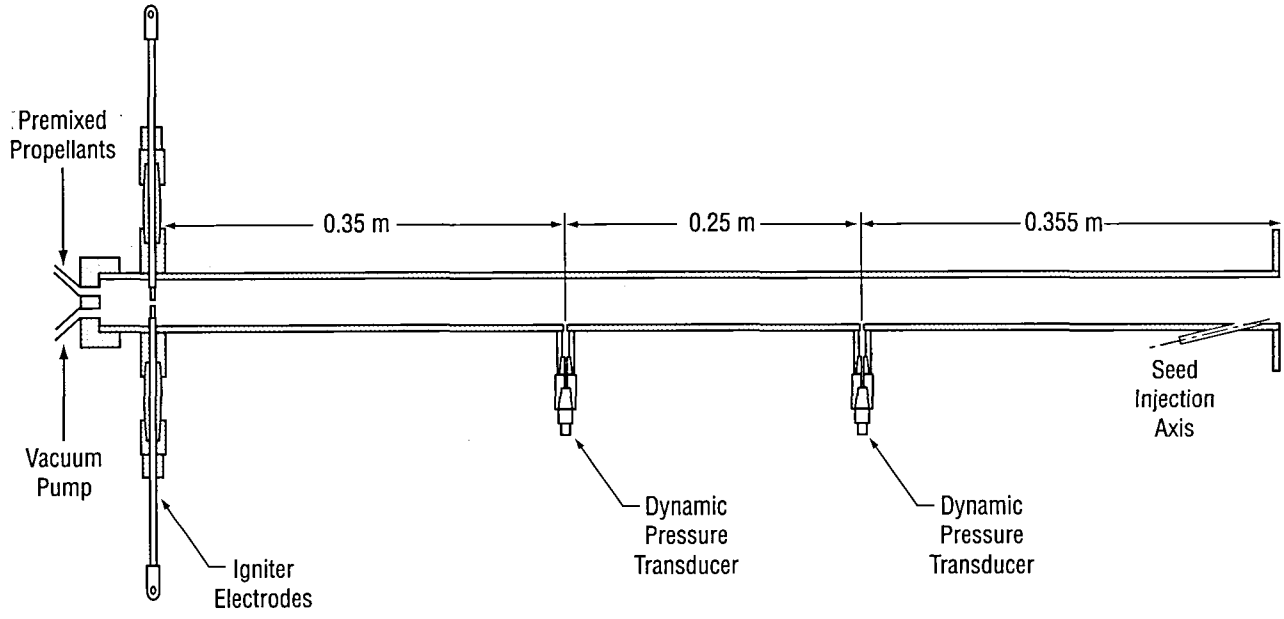

Figure 8. Schematic of the 1-m-long, laboratory-scale pulse detonation tube with 2.54-cm bore.

A pair of high-voltage igniter electrodes were fabricated from copper (Cu) pins with tungsten (W) tip inserts and located near the closed end of the tube. The tip of the igniter cathode was ground to a point to increase the local electric field intensity and thereby reduce the required breakdown voltage across the 3-mm gap. The discharge energy for directly initiating the combustion detonation wave is created by discharging the energy stored in an inductive-resistive-capacitive (LRC) circuit that is closed using a solenoid-operated mechanical switch. The oscillating electric field that drives the gas discharge was observed to decay completely within 100 μsec. The circuit discharges a 2-μF energy storage capacitor which has been precharged to 10 kV, yielding an ignition energy source of magnitude $W_{ign} = {}^1/_2\ CV^2 \sim 100$ J. This value exceeds the minimum ignition energy necessary for direct initiation of C_2H_2/O_2 mixtures by several orders of magnitude.[10] This level of ignition energy provides assurance that true detonation conditions are attained.

Two dynamic pressure transducers are mounted in the tube at roughly equal distances from either end such that the separation distance between them is exactly 0.25 m. These sensors provide an indication of detonation wave strength and are used for time-of-flight measurements of detonation wave speed. For a data sampling rate of 200 kHz, an uncertainty of ± 5 μsec is encountered in the time-of-flight measurement.

3.1.2 Atomizing Seed Injector

An electrically activated atomizing fuel injector from an automotive engine was adapted for injection of ionization seed. The injector was mounted to the detonation tube and oriented so that the spray cone was directed downstream into the channel region. A 30-percent solution (by mass) of CsOH in a methanol carrier was used for seeding. In conducting each test, the pressurized injector for 50 msec was first activated and then the ignition trigger was delayed by 100 msec. Based on a calibrated volumetric injection rate of 3 cm^3/sec, it was estimated that 0.15 cm^3 of seed solution was injected per shot. It was impossible to ascertain the actual seed fraction in the channel, however, due to poorly defined atomization characteristics, attachment of the seed material to the wall, and uncertainty in the seed distribution.

3.1.3 Plasma Diagnostic Channel

A plasma diagnostic channel was also designed and fabricated to quantify the electrical properties of the ionized gas behind the detonation front. This short length, axisymmetric diagnostic channel, which has the same internal diameter as the detonation tube, is shown in figure 9. The main body is machined from G–11 phenolic and is fitted with a set of 1.6-mm copper electrode segments to which a preset electric potential can be applied. These electrodes are mounted flush with the wall and maintain a contact angle of 60° with the flow. The channel is also equipped with two tungsten wire electrostatic probes for measuring the local plasma potential in the core. They are located 5 mm above the anode and cathode surfaces, respectively. Together, the discharge electrodes and electrostatic probes form a four-electrode electrical conductivity probe.[18] A tap for a dynamic pressure transducer is located at the same axial location. In addition, a sapphire window port was integrated into the design so that the gas discharge process and detonation wave passage could be observed optically. The diagnostic channel was fabricated for direct mating with the detonation tube.

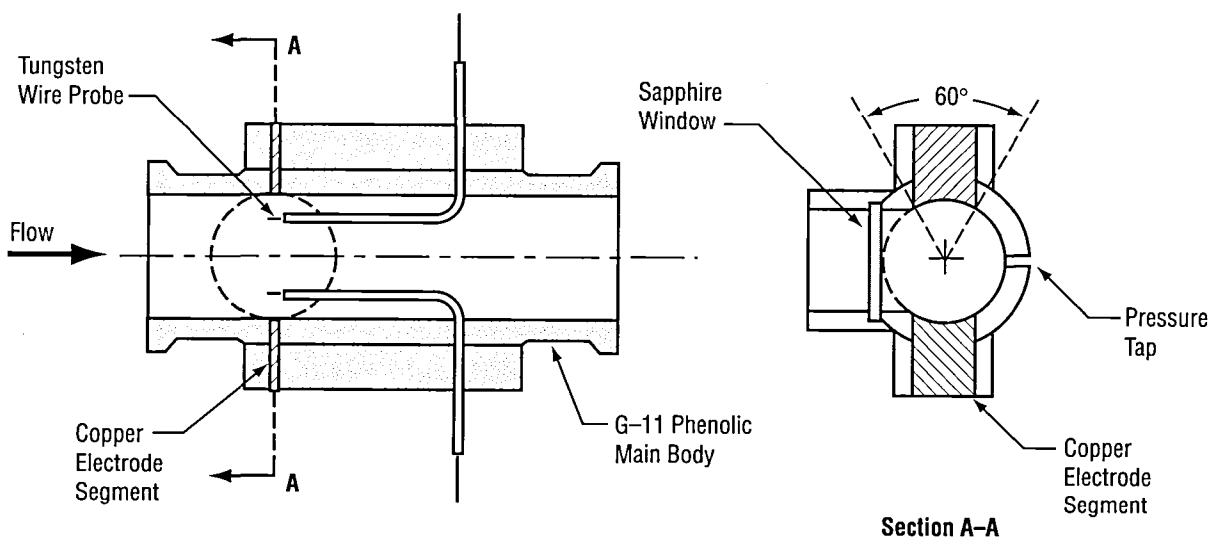

Figure 9. Schematic of windowed axisymmetric plasma diagnostic channel. Note that the wall-mounted discharge electrodes can be combined with the electrostatic probes in the core to form a four-electrode electrical conductivity probe.

3.1.4 Laboratory Magnets

A permanent magnet assembly (0.6 T) and a laboratory electromagnet (0.95 T) were custom fabricated to support testing efforts. The permanent magnet is composed of individual segments as shown in figure 10. Each segment is 2 in. wide and contains eight 2 × 2 × 1 in. low-grade, rare Earth magnetic blocks (BH_{max} = 35 MGOe) and four 2 × 2 × 1/2 in. high-grade, rare Earth magnetic blocks (BH_{max} = 45 MGOe). A total of six segments combine to form a 30-cm-long, permanent magnet assembly that provides a uniform magnetic induction of 0.6 T over a 3.8-cm air gap. The laboratory electromagnet is shown schematically in figure 11. The bore for this magnet is 46 cm long and has a 5-cm air gap. The maximum magnetic induction in the bore is 0.95 T at full design current.

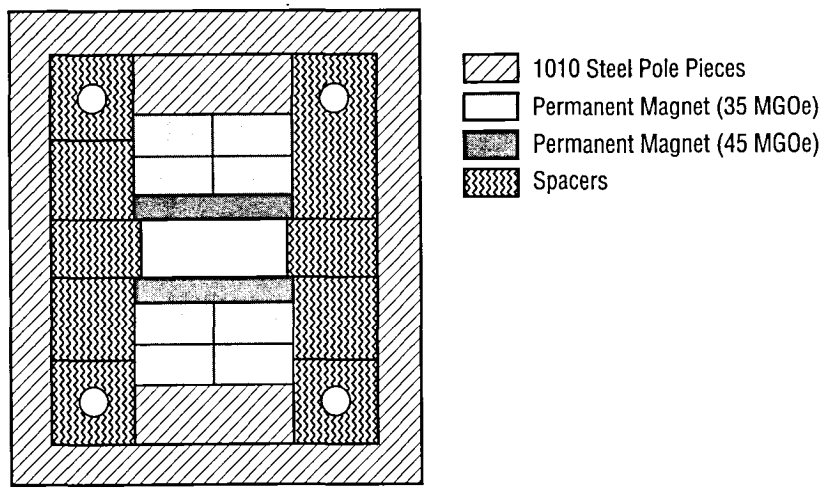

Figure 10. Cross section of permanent magnet segment. Six segments are combined to form a 30-cm-long assembly having a uniform magnetic induction of 0.6 T over a 3.8-cm air gap.

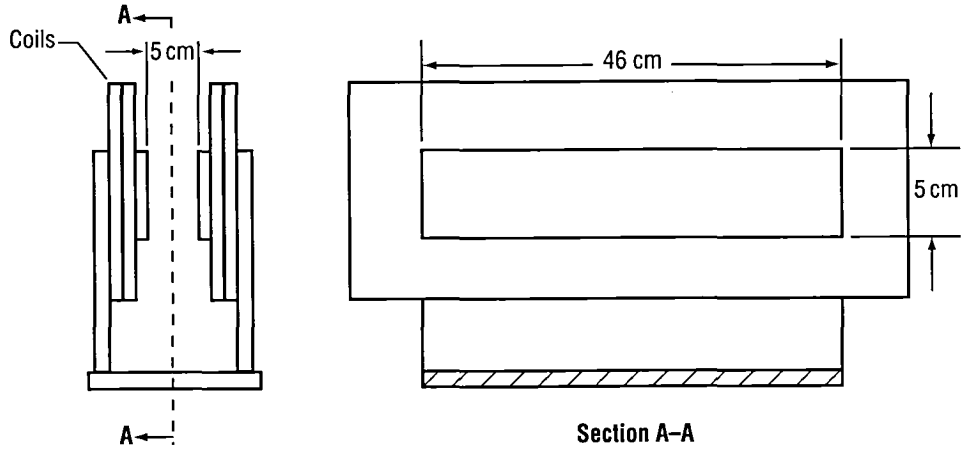

Figure 11. Schematic of the laboratory electromagnet. The magnet bore is 46 cm long with an air gap of 5 cm. The magnetic induction in the bore is 0.95 T at full design current.

3.1.5 Faraday MHD Channel

A continuous-electrode Faraday MHD channel was also designed and fabricated to fit the available laboratory magnets. This constant-area channel, shown in figure 12, has an active MHD length of 30 cm. The internal flow passage is rectangular in shape with a 2.54-cm height between electrodes and a 2-cm width between sidewalls. The main body of the channel is fabricated from G–11 phenolic, as is the area transition adapter connecting the tube to the channel. The copper alloy electrodes include pressure taps at four locations along the active channel length.

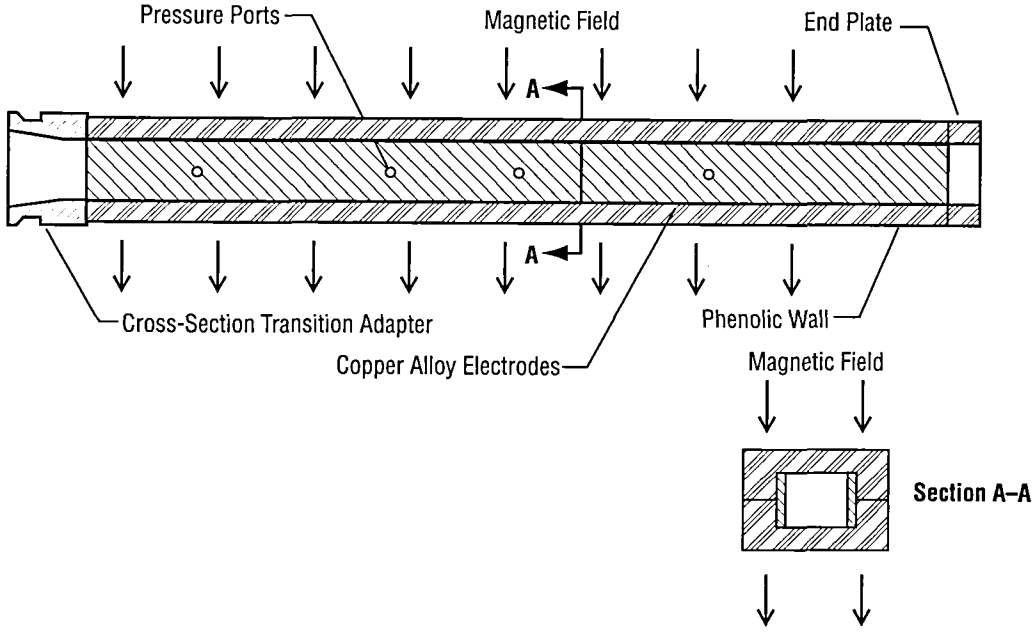

Figure 12. Schematic of the 0.3-m-long, continuous-electrode Faraday MHD channel. Active region is 2.54 cm in height and 2 cm in width.

3.1.6 Experiment Control and Signal Acquisition

A PC-class computer with appropriate I/O hardware was used to sequence and control the experiments and acquire four channels of high-speed data at a sampling rate of 200 kHz per channel. A 50-MHz, two-channel digital oscilloscope was also utilized to capture fast signal transients. High-speed diagnostic measurements available for physical interpretation include the following: Time-resolved thrust profiles as a means of deducing I_{sp} performance; static pressure fluctuations at the wall to define the speed and strength of the combustion detonation wave; radiative emission through the window port of the diagnostic channel for additional definition of detonation wave morphology and structure; electrostatic probe voltages for measuring local plasma potential relative to the cathode; anode-to-cathode voltages and currents in the plasma diagnostic channel circuit as a means of deducing the electrical properties of the ionized gas; and load voltages and currents in the MHD channel circuit as a means of deducing power extraction characteristics.

3.2 Electrodynamic Model

A simple, first-order electrodynamic model was developed as an aid to the interpretation of experimental results and as a basis for developing generalized scaling laws. In this model, it is assumed that a uniform slug of burned ionized gas moves with velocity **u** through a channel of height h that is subjected to an applied magnetic induction **B**. Wall electrodes directly couple MHD interaction in the flowing plasma with an LRC active loading circuit. In general, the slug thickness δ may be less than the active channel length L. A uniformly distributed current density **j** in the plasma slug is assumed, and Hall effects are neglected due to the very high-pressure levels experienced behind the combustion detonation wave. Furthermore, the magnetic Reynolds number is assumed to be much less than 1, and flux compression effects were neglected. The electrodynamic model and potential level diagram are shown in figure 13. The active loading circuit includes the possibility of precharging the capacitor to an applied voltage v_0 as a means of simulating a higher effective magnetic induction, $\mathbf{B}_{eff}$.

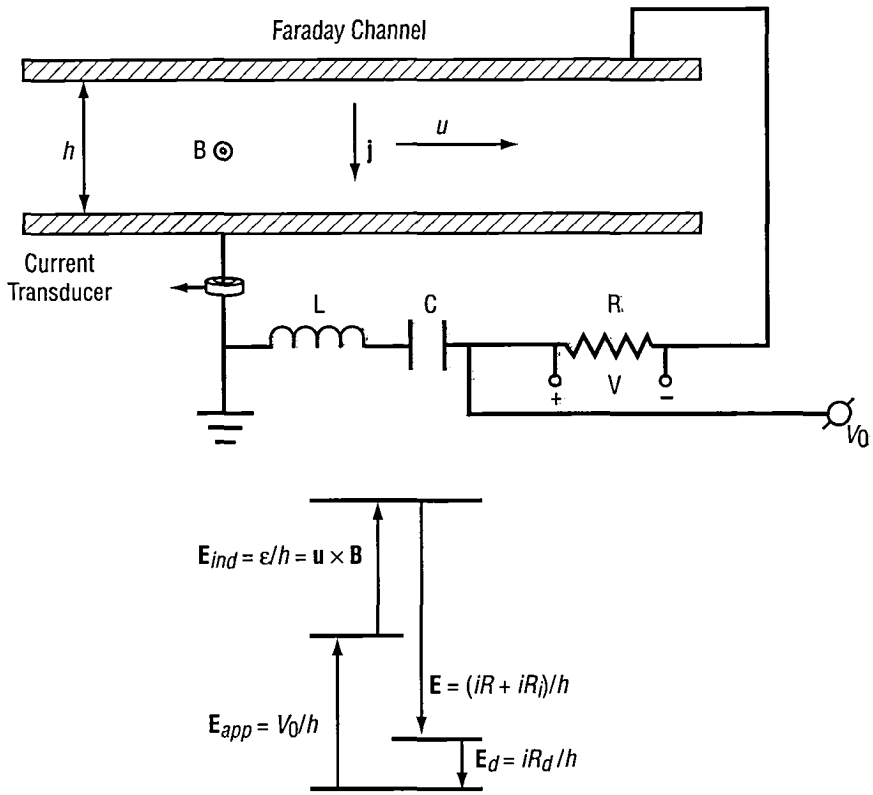

Figure 13. LRC active loading circuit and electric potential level diagram for idealized electrodynamic model.

The effective induced electric field $\mathbf{E}_{eff}$ in the channel is the sum of the induced Faraday field associated with the applied magnetic induction, $E_{ind} = |\mathbf{u} \times \mathbf{B}| = \varepsilon/h$, and the applied field, $E_{app} = v_0/h$. Thus, the effective induced potential in the channel may be written as

$$\varepsilon_{eff} = \varepsilon + v_0 = uBh + v_0 = uB_{eff}h \quad , \tag{32}$$

where

$$B_{eff} = B + \frac{v_0}{uh} \quad . \tag{33}$$

Requiring that the current have a positive magnitude in the direction of $\mathbf{u} \times \mathbf{B}$, Kirchoff's voltage law implies that the effective induced electromagnetic force (emf) $\varepsilon_{eff} = uB_{eff}h$ be balanced by voltage drops resulting from the external load R, internal resistance of the plasma R_i, and a lump potential loss $v_d = iR_d$:

$$\varepsilon_{eff} = uB_{eff}h = iR + iR_i + iR_d = V + jh/\sigma + v_d \quad , \tag{34}$$

where the current density, $j = i/A$, and the electrical conductivity, $\sigma = h/(AR_i)$, have been introduced. The lump loss term v_d is introduced to account for plasma nonuniformities, near-electrode potential drops, emission losses, current concentrations, as well as possible current leakage and shortings.[19] It is assumed that $v_0 \approx$ constant during passage of the plasma slug, and because the inductance in the loading circuit is extremely low, inductive energy storage terms have been neglected. Thus, equation (34) may be further manipulated to obtain

$$uB_{eff} = V/h + j/\sigma + v_d/h = E + j/\sigma + E_d \quad , \tag{35}$$

where i is the load current and V is the terminal voltage measured across the load. Solving equation (35) for j yields the generalized Ohm's law for the generator:

$$j = \sigma\left[uB_{eff} - E - E_d\right] \quad . \tag{36}$$

Following a modeling strategy analogous to Wu,[19] a dimensionless voltage drop Δ is defined as

$$\Delta = v_d/uB_{eff}h \quad . \tag{37}$$

This engineering parameter represents a direct measurement of the voltage drop losses relative to the effective emf of the generator.

For an MHD generator, the load factor K is defined as

$$K = \frac{\text{electric power delivered to load}}{\text{useful electric power generated}} = \frac{i^2R}{i^2R + i^2R_i} \tag{38}$$

and elimination of v_d for Δ yields the relation

$$K = \frac{iR}{iR + iR_i} = \frac{V}{uB_{eff}h - v_d} = \frac{E}{uB_{eff}(1-\Delta)} \quad . \tag{39}$$

By substituting equations (37) and (39) into the generalized Ohm's law, an expression is obtained for the current density in the generator:

$$j = \sigma u B_{eff}(1-\Delta)(1-K) \quad . \tag{40}$$

In addition, an expression for the generator power density follows from the basic definition $\mathcal{P} = \mathbf{j} \bullet \mathbf{E}$ and from use of equations (39) and (40) to eliminate E and j:

$$\mathcal{P} = \mathrm{j} \bullet \mathrm{E} = \sigma u^2 B_{eff}^2 (1-\Delta)^2 K(1-K) \quad . \tag{41}$$

The maximum power density occurs when $d\mathcal{P}/dK = 0$ such that $K = {}^1/_2$ for optimum performance. It should be clear from equation (41) that when the induced emf is limited due to small channel height and/or low magnetic induction, the lump potential loss v_d can have a profound affect on generator performance.

The Lorentz body force acting on the plasma slug may be defined in terms of the charged particle drift velocity **w**:

$$\mathbf{f} = nq(\mathbf{w} \times \mathbf{B}) = \mathbf{j} \times \mathbf{B} \tag{42}$$

and substitution of equation (40) into equation (42) yields the actual Lorentz body force experienced by the plasma slug:

$$f = |\mathbf{j} \times \mathbf{B}| = \sigma u B_{eff} B(1-\Delta)(1-K) < \left|\mathbf{j} \times \mathbf{B}_{eff}\right| \quad . \tag{43}$$

Thus, for the active loading circuit, $f \propto B_{eff}B$ assuming all other factors remain constant. However, for true similarity, the Lorentz body force should vary in proportion to B^2_{eff}, not BB_{eff}, and the MHD interaction level is too small by the factor $B_{eff}/B = 1 + v_0/(uBh)$.

More directly stated, the magnetic interaction parameter S (work done by Lorentz force/inertial energy of flow field) based on the use of an effective magnetic induction is less than that required for proper simulation of the push work; that is,

$$S = R_m R_h = \frac{\sigma_0 L_0 B_{eff} B_0}{\rho_0 u_0} < \frac{\sigma_0 L_0 B_{eff}^2}{\rho_0 u_0} = S_{\text{required}} \quad , \tag{44}$$

where R_m (Lorentz force/magnetic body force) is the magnetic Reynolds number, R_h (magnetic body force/ inertial force) is the magnetic force number, and the subscript zero refers to reference conditions. The actual rate at which the ionized gas does push work in the actively loaded channel is

$$\mathcal{P}_p \approx fu = \sigma u^2 B_{eff} B(1-\Delta)(1-K) \quad . \tag{45}$$

When C=0 and there is no applied voltage, $B_{eff} = B$ and the passive load model is recovered.

3.3 Experimental Results

3.3.1 Detonation Characteristics

As a prelude to operating the detonation tube, detonation calculations were carried out using the NASA SP–273 chemical equilibrium code.[20] The stoichiometric mixture ratio was based on the combustion products being either carbon dioxide or water, and the initial static pressure and temperature in the unburned gas was p_1=1 atm and T_1=300 K. Assuming C-J detonation wave structure, this program computes, among other parameters, the pressure/temperature ratio across the detonation front, the detonation wave velocity D relative to the duct, and the speed of sound of the burned gas a_2 relative to the detonation wave. For C-J conditions, the burned gas velocity is sonic relative to the detonation wave (i.e., M_2 =1), and $u_2 = a_2 = \sqrt{(\gamma_2 R_2 T_2)}$. Then, it is possible to deduce the burned gas velocity relative to the tube using the relation $u_b = D - u_2 = \quad D - a_2$ where u_b corresponds to the slug velocity in our electrodynamic model. The major results, summarized in table 2, provide a baseline performance benchmark for our experiments.

Table 2. Summary of calculated denotation wave properties.

D (m/sec)	2,425
a_2 (m/sec)	1,317
u_b (m/sec)	1,100
p_2/p_1	33.64
T_2/T_1	14.04

The computed detonation wave speed is in good agreement with widely accepted experimental measurements.[21] A static pressure p_2 = 33.64 atm (495 psia) and a static temperature T_2 = 4,200 K behind the detonation wave based on initial conditions in the tube are expected.

Experiments were then conducted in our apparatus to confirm the attainment of true detonation conditions. As an example, representative pressure waveforms acquired from the dynamic pressure transducers during a typical shot are presented in figure 14. The slightly elevated pressure levels near the ignition source are attributed to overdriven detonation as caused by use of an extremely high ignition energy (≈100 J). Once the detonation wave has traversed two-thirds the length of the tube, however, C-J conditions are fully attained, and the pressure rise across the detonation front is found to be in close agreement with the baseline theoretical prediction. As further evidence, note that the cross correlation of these waveforms yields a time delay of 105 μsec and a detonation wave speed relative to the tube of 2,380 m/sec. This quantity is also in good agreement with the baseline calculations. Repeated experiments showed little variation in the preceding results, providing confidence that true detonation conditions were being reliably achieved.

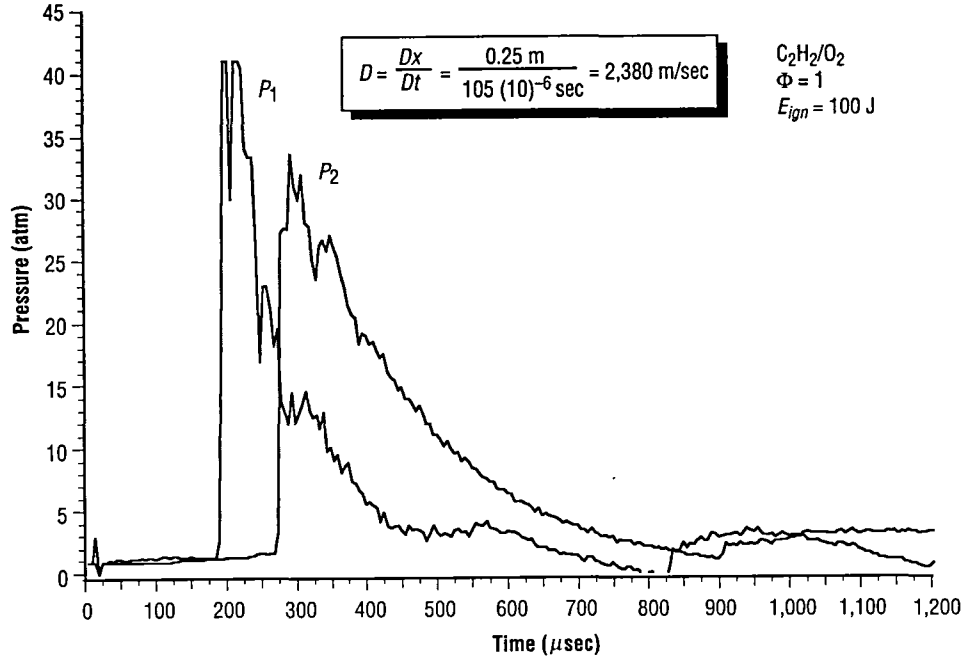

Figure 14. Representative measured pressure waveforms in the detonation tube during a typical shot.

3.3.2 Plasma Diagnostics

With the plasma diagnostic channel attached to the end of the detonation tube, further experiments were conducted to quantify the ionization properties of the burned gas following the detonation front. Of utmost interest were (1) the level of electrical conductivity achieved, (2) the magnitude of near-electrode potential losses, and (3) the definition of structural features.

In these experiments, an electric breakdown potential of 100 V was applied between the wall electrodes during passage of the detonation wave. The resulting discharge of current through the ionized gas allowed deduction of bulk electrical properties from the measured electrostatic probe voltage waveforms and the anode-to-cathode current waveforms. Although highly intrusive, this technique provides an effective measurement of major electrical parameters of engineering interest.

The single, most important parameter indicating ionization quality is the electrical conductivity. In this work, two intrusive probing methods were utilized for determining an effective bulk value based on Ohm's law, $j = \sigma E$. They are classified as two- and four-electrode probes, respectively.[18] Application of these probing methods can lead to dubious results, however, due to uncertainty in the current distribution within the ionized gas. This uncertainty in current distribution makes the accurate assessment of current density and derived quantities such as electrical conductivity problematic.

Reliable deduction of these electrical parameters requires careful consideration of electrode geometry and probe configuration. When using point electrodes, for example, fundamental theoretical considerations and a vast array of empirical evidence has demonstrated that the current tends to uniformly diffuse into a

spherical distribution having a diameter equal to the anode-to-cathode gap in the ionized gas.[22] Based on symmetry arguments for the thin electrode segments used in the diagnostic channel, it is assumed, therefore, that the current will uniformly diffuse into a circular cylinder having a diameter equal to the channel height h and a length equal to the electrode width w. This geometry is illustrated in figure 15.

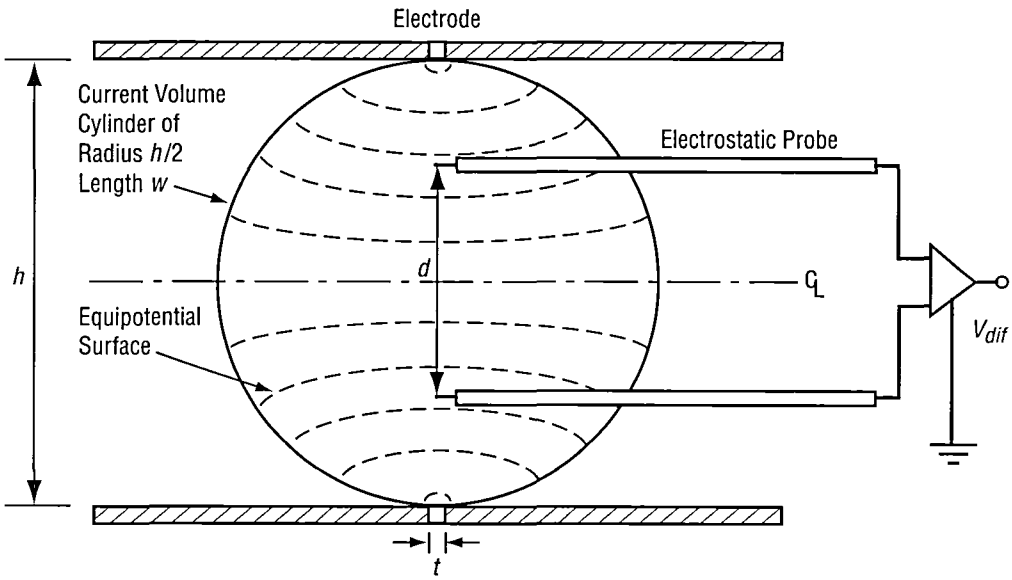

Figure 15. Illustration of the assumed current distribution between discharge electrodes in the plasma diagnostic channel.

The electric field between the electrodes can be modeled using two-dimensional line sources where the electric potential ϕ at any point (x,y) from the centerline of the electrodes and the centerline of the channel is obtained by summing the contribution due to each line source:

$$\phi = \Lambda \ln\sqrt{x^2 + (h/2 - y)^2} - \Lambda \ln\sqrt{x^2 + (h/2 + y)^2} \quad . \tag{46}$$

The constant Λ represents the source strength and can be evaluated by imposing the known voltages on the top and bottom electrodes. The electric field vector $\mathbf{E}$ can be determined from the relation $\mathbf{E} = -\text{grad}\ \phi$. The equipotential surfaces within the assumed cylindrical current volume are illustrated schematically in figure 15.

3.3.2.1 Two-Electrode Probe. In the two-electrode method, consider first a cross-section of the assumed cylindrical current volume and define the current density j through an equipotential surface A_{es} as

$$j = \frac{i}{A_{es}\xi} \quad , \tag{47}$$

where i is the measured total current and ξ has been introduced as an efficiency coefficient of order unity. As a simplification to the analysis, approximate the area of the equipotential surfaces as the product of the cylinder chord c and the electrode width w:

$$A_{es} \approx wc = w2\sqrt{h\zeta - \zeta^2} \quad , \tag{48}$$

where ζ is the radial distance from the electrode surface to the chord, and $A_{es} = wh$ when $\zeta = h/2$. Upon substituting Ohm's law, an expression is obtained for the local electric field in the form

$$E = \frac{i}{w\xi\sigma 2} \frac{1}{\sqrt{h\zeta - \zeta^2}} \quad . \tag{49}$$

Then, integrate for the applied voltage across the channel, using equation (49):

$$v_{app} = 2 \int_0^{h/2} E \, d\zeta = \frac{i}{w\xi\sigma} \int_0^{h/2} \frac{d\zeta}{\sqrt{h\zeta - \zeta^2}} \quad . \tag{50}$$

Evaluation of this integral yields the final desired expression for electrical conductivity in terms of the primary measurement parameters:

$$\sigma = \frac{\pi}{2} \frac{i}{v_{app} w\xi} \quad . \tag{51}$$

3.3.2.2 Four-Electrode Probe. Unfortunately, the two-electrode probe tends to suffer from near-electrode potential drops and nonohmic contact resistances, and a four-electrode probe is usually recommended. In the four-electrode probe, a pair of electrostatic probes are introduced between the anode and cathode to measure the voltage drop v_{dif} over a distance d in the core of the flow. With this configuration, the parasitic resistance problems are minimized.

The critical assumption is the definition of the cross-sectional area for computing current density in the core. Here, the cross-section of the current volume cylinder at the centerline is taken as the effective area such that $A_{eff} = wh$. Thus, the effective current density in the core j_{eff} takes the form

$$j_{eff} = \frac{i}{A_{eff}\xi} = \frac{i}{wh\xi} \quad . \tag{52}$$

The expression for electrical conductivity using the four-electrode configuration follows from a direct application of Ohm's law:

$$\sigma = \frac{j_{eff}}{E} = \frac{i}{wh\xi} \frac{d}{v_{dif}} \quad . \tag{53}$$

3.3.2.3 Ionization Quality/Structure. A seven-waveform ensemble average of the effective current density in the diagnostic channel, as computed from equation (52), is shown in figure 16. In this work, ξ is taken to be unity. These measurements demonstrate the emergence of primary and secondary wave structures. The primary wave is associated with the passage of the burned gas behind the detonation front, but the physical mechanism responsible for the trailing secondary wave is not clear. The emergence of a conductive secondary wave structure has been observed in previous detonation experiments with oxy-acetylene mixtures.[4,23–25] Generally speaking, these experiments indicate a secondary wave structure which may be associated with delayed chemical reactions behind the detonation front. As such, the induction period never exceeded more than a few hundred microseconds. In figure 16, however, the time delay between the primary and secondary waves is rather long (≈1.5 msec), and the appearance of the secondary waveform shows a temporal correlation with the extreme tail of the measured pressure waveform. Therefore, the secondary waveform observed here is more probably associated with flow reversal in the channel. The peak current density in the primary and secondary waves was roughly 2 and 0.5 A/cm^2, respectively.

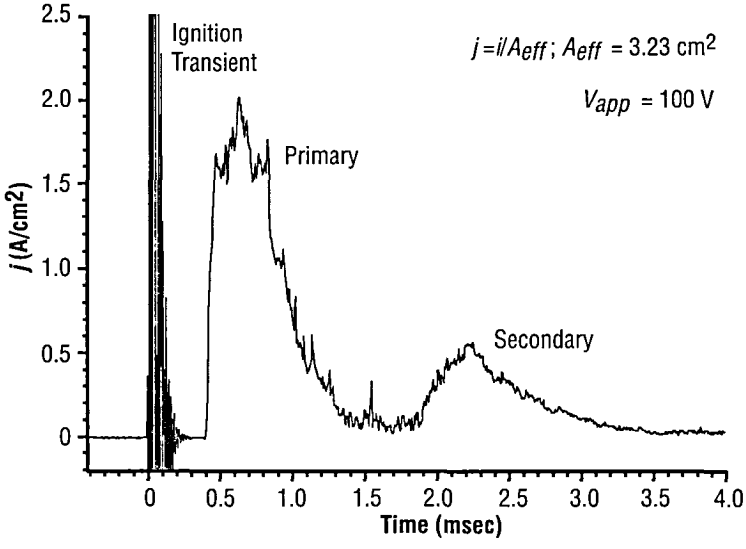

Figure 16. Seven-waveform ensemble average of the effective current density in the plasma diagnostic channel. Note the delayed appearance of a secondary wave structure.

Normalized seven-waveform ensemble averages of static pressure and radiative emission in the diagnostic channel are shown in figure 17. In this case, the hump riding on the trailing edge of the pressure waveform is indicative of a secondary compression wave similar to that observed by Cher and Kistiakowsky.[24] Radiative emission integrated over the optical region is very constant during passage of the primary conductive wave, seemingly suggestive of fairly uniform thermal conditions; however, the measured electrical conductivity, presented below, does not corroborate this interpretation.

A seven-waveform ensemble average of the differential electrostatic probe voltage v_{dif} is shown in figure 18. Only data corresponding to passage of the primary wave were captured. Note that the voltage drop between probes was ≈40 V during this event. By assuming $v_d \approx v_{app} - v_{dif}$, it was possible to estimate the dimensionless voltage drop in the channel using equation (37) where $B_{eff} = v_{app}/uh$. This estimation yielded $\Delta \approx 0.6$.

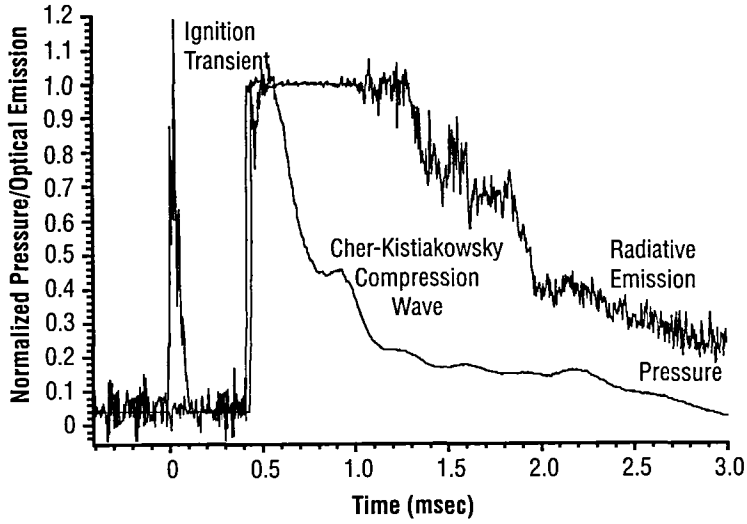

Figure 17. Seven-waveform ensemble average of static pressure and radiative emission in the plasma diagnostic channel. Waveforms have been normalized using peak values in the detonation front. Note the emergence of a receding Cher-Kistiakowsky secondary compression wave.

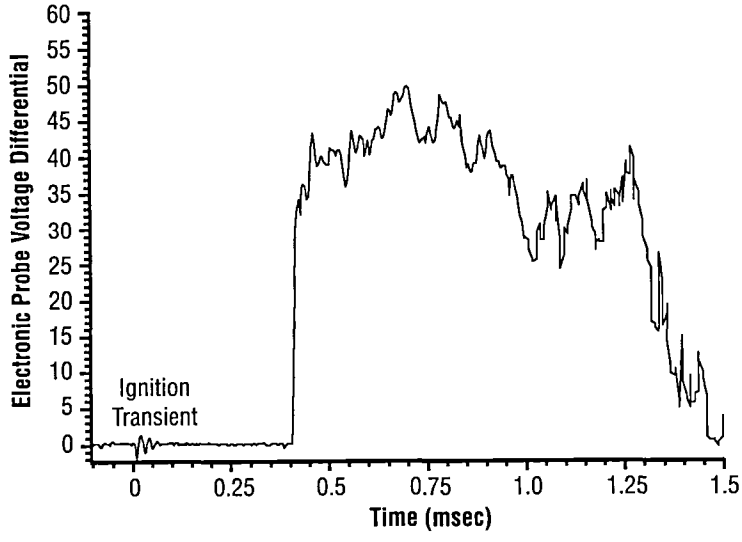

Figure 18. Seven-waveform ensemble average of the electrostatic probe voltage differential in the plasma diagnostic channel.

Ensemble-averaged, electrical conductivity waveforms are shown in figure 19 based on two- and four-electrode probing techniques. Agreement between the two methods is very good. The peak electrical conductivity in the primary wave is seen to be ≈6 S/m. For comparative purposes, calculations were carried out for the electrical conductivity and electron number density in the burned gas as a function of the seed mole fraction. This was accomplished using a modified version of NASA SP–273 chemical equilibrium code in which the plasma electrical transport properties are computed according to Frost.[26] The results are shown in figure 20.

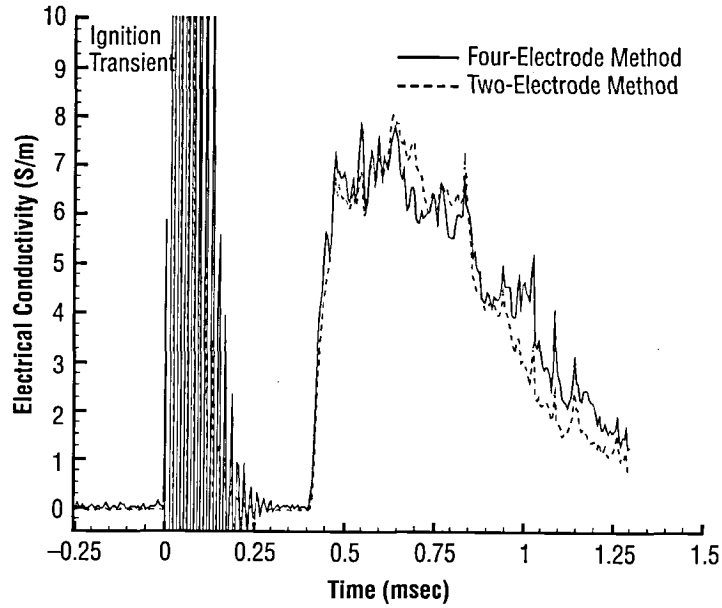

Figure 19. Seven-waveform ensemble average of the electrical conductivity in the plasma diagnostic channel based on both two- and four-electrode probing techniques.

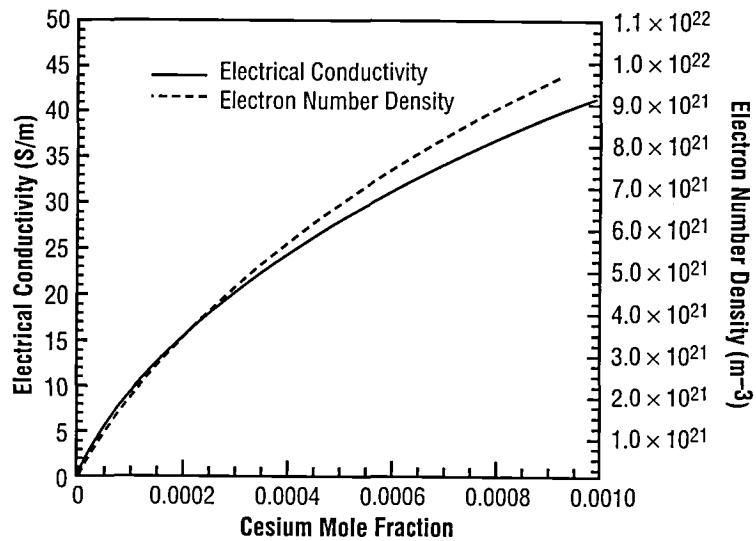

Figure 20. Computed electrical conductivity and electron number density behind the detonation front based on a modified version of the NASA SP–273 chemical equilibrium code where plasma electrical transport properties are computed according to Frost.

3.3.3 MHD Power Extraction

MHD power extraction experiments were conducted with the short-length, continuous-electrode Faraday channel attached to the detonation tube and placed in the bore of the magnet assemblies. In these experiments, the channel was connected to the active loading circuit shown in figure 13 in order to simulate higher effective magnetic induction. Our principal objectives were as follows: (1) To demonstrate pulse

detonation-driven MHD energy conversion, (2) to map the load line characteristics of the generator, and (3) to estimate energy density characteristics for engineering scaling purposes.

3.3.3.1 Open-Circuit Voltage/Burned Gas Velocity. The first task was to acquire open-circuit characteristics of the generator by applying a very high load impedance with the capacitor removed from the circuit. Figure 21 shows a typical terminal voltage waveform under these conditions, where the waveform represents a direct measurement of the peak Faraday potential in the generator, $V_{OC} = uBh \approx 10$ V. Obviously, the small scale of the device greatly inhibits performance in that the near-electrode potential drop is of the same order as the Faraday potential. Dividing this waveform by the known magnetic induction (0.6 T) and the channel height (0.0254 m), one can deduce an effective burned gas velocity relative to the tube of $\langle u_b \rangle \approx 660$ m/sec. This value can be compared with the theoretical equilibrium prediction specified in table 1 (1,100 m/sec). The effective burned gas velocity is lower because the velocity behind the detonation wave must decay to zero at the closed end of the tube.

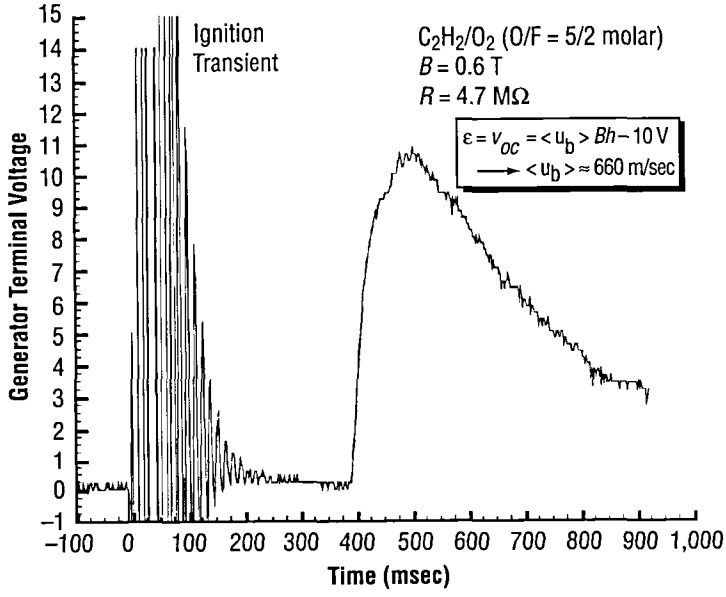

Figure 21. Generator terminal voltage waveform under open-circuit loading conditions. Division of this waveform by *Bh* yields an effective burned gas velocity waveform in the channel.

3.3.3.2 Load-Line Characteristics. The load-line characteristics of the generator were mapped out for six values of effective magnetic induction v_0: 0.6, 0.95, 1.5, 2.4, 3.3, and 4.2 T. For each effective magnetic induction, current waveforms for the following set of load impedance values were measured: 0, 0.0175, 0.098, 1, 5, 10, and 100 Ω. Representative results are shown in figure 22 for $B_{eff} = 1.5$ T. As expected, the peak current attains its maximum value under short-circuit conditions and falls with increasing load impedance. Also note the emergence of a delayed, relatively weak secondary pulse which is associated with the secondary gas-dynamic wave identified in figure 17.

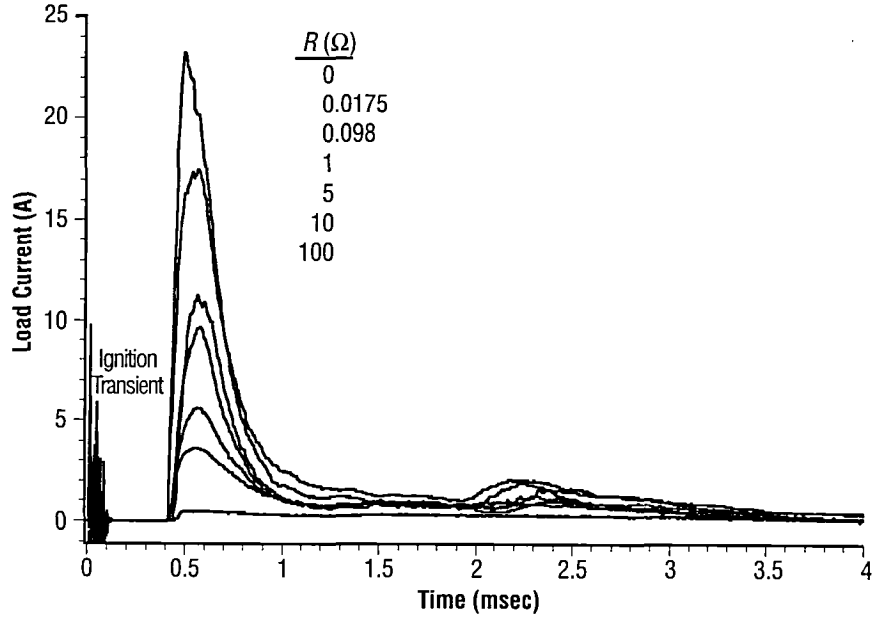

Figure 22. Measured current waveforms for various load impedances with B_{eff} = 1.5 T. Peak current scales inversely with load impedance.

Generator load lines were constructed based on measured peak values for current and load voltage. The results, normalized with respect to the short-circuit current and the open-circuit voltage, are shown in figure 23. The characteristic shape exhibits linear features away from the extreme loading conditions. The cause of the highly nonlinear behavior near short-circuit conditions is still not understood.

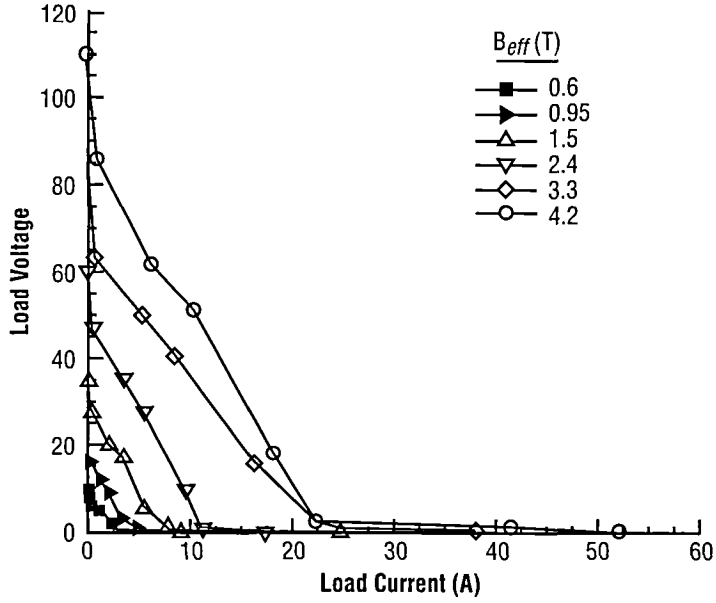

Figure 23. Measured load-line characteristics of the pulse detonation MHD generator. Solid symbols denote true simulation conditions (i.e., $B = B_{eff}$).

3.3.3.3 Energy Density Scaling Parameter. From an engineering point of view, it is advantageous and useful to express the power extraction characteristics of the generator in terms of a performance-related scaling parameter. Once quantitative estimates are developed for this parameter, it is possible to project device performance at practical scales. Although it is difficult to extrapolate the performance of MHD devices from laboratory scales, where boundary layer losses dominate, to a scale suitable for practical application, where core flow processes dominate, this approach is adopted as a conservative estimate of scaling effects. Under virtually all circumstances, this approach will tend to underpredict performance and will usually represent a worst-case scenario. The prediction can therefore be treated as an effective lower bound on anticipated performance.

Since electrical power output is the performance parameter of primary interest in MHD generators, development is begun with the following definition:

$$\frac{dW}{dt} = u\frac{dW}{dx} = \mathcal{P}wh\delta \quad , \tag{54}$$

where W represents electrical work in Joules and the power density $\mathcal{P}$ was obtained in equation (41). The electrical work per unit channel length per detonation pulse can therefore be written as

$$\frac{dW}{dx} = \frac{\mathcal{P}wh\delta}{u} \approx \frac{W_D}{L} \quad . \tag{55}$$

Here, L is the active length of the MHD channel and W_D represents the electrical energy transferred per detonation pulse. Further note that W_D can be empirically evaluated by integrating over the measured output waveform of the generator:

$$W_D = \int i^2 R\,dt + \mathcal{L}\int i\frac{di}{dt}dt \approx \int i^2 R\,dt \quad , \tag{56}$$

where the inductance $\mathcal{L}$ is very small in our circuit and can be neglected.

Equation (55) can now be manipulated to obtain the desired energy density scaling parameter in the form

$$\frac{W_D}{whL} = \frac{\mathcal{P}\delta}{u} \quad . \tag{57}$$

This parameter has units of J/m^3 and represents the electrical energy produced per unit channel length per unit channel height per unit channel width per detonation. By eliminating $\mathcal{P}$ using equation (41), one arrives at the final working relation:

$$\frac{W_D}{whL}(1-\Delta)^{-2} = \delta u B^2 K(1-K) \quad . \tag{58}$$

Note that the parameters on the right-hand side of equation (58) are assumed to be independent of device scale. Thus, once the energy density W_D/whL is empirically evaluated and one is able to make appropriate assumptions concerning the scaling of Δ, it becomes possible to extrapolate performance at increased scales.

A comparison of measured and theoretical predictions for the energy density scaling parameter is presented in figure 24 as a function of load impedance. The empirical value was obtained by integrating equation (56) using measured current waveforms and dividing by the known active channel volume. The theoretical predictions were computed from equation (58) using the following device parameters: $\Delta = 0.6$, $\delta = 0.3$, $\sigma = 6$ S/m, $u = 1{,}100$ m/sec, $B = B_{eff} = 0.6 + v_0/uh$ T, and $h = 0.0254$ m. Agreement is reasonably good given the uncertainty in parameter values. The measured peak electrical energy density ranged from 10 to 10^3 J/m^3 when the effective magnetic induction was varied from 0.6 to 4.2 T. Clearly, the performance of this MHD device is limited by scale and near-electrode potential losses.

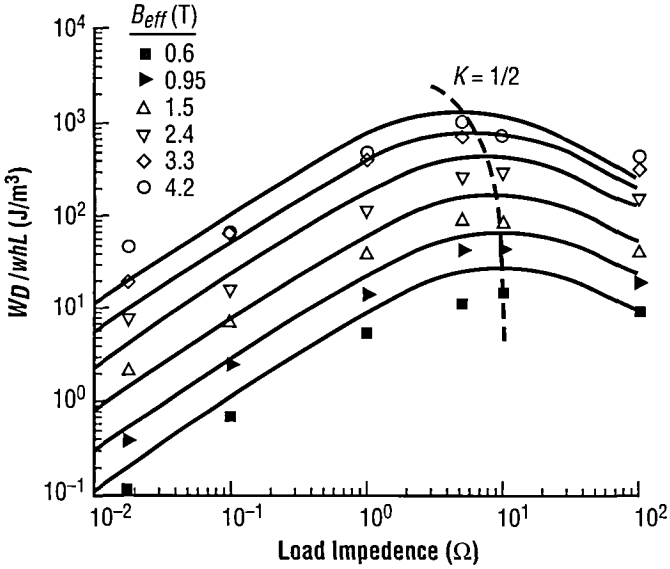

Figure 24. Comparison of measured and theoretical predictions for the energy density scaling parameter as a function of load impedance. The theoretical predictions are shown as curves. Device parameters used in the calculations were as follows: $\Delta = 0.6$, $\delta = 0.3$, $\sigma = 6$ S/m, $u = 1{,}100$ m/sec, $B_{eff} = 0.6 + v_0/uh$ T, $h = 0.0254$ m. Optimum power extraction occurs when $K = 1/2$. Solid symbols denote true simulation conditions (i.e., $B = B_{eff}$).

The results also show peak power extraction shifting from a load impedance of 10 Ω, when $v_0 = 0$ V, to 5 Ω, when $v_0 = 100$ V. This shift is associated with decreasing internal plasma resistance as the effective magnetic induction and Joule dissipation increase. That is, optimum electrical power extraction always occurs when the load impedance and the internal impedance of the generator are matched.

At this point, recall that the magnetic interaction parameter S based on an effective magnetic induction is less than that required for accurate simulation of the MHD interaction level. That is, the push work done by the working medium in these experiments is much lower than would be required if the magnetic induction was equivalent to the applied field. In order to justify the extrapolation of these results to the practical case

where $B = B_{eff}$, a forced assumption is made that the enthalpy extraction achievable in the nonsimulated case will be high enough to provide the required push work. It is also necessary to assume weak coupling between MHD interaction level and burned gas velocity.

3.3.3.4 Extrapolation of Performance to Practical Scales. The performance of small MHD devices tends to suffer from severe boundary layer losses, as evidenced by our experimental results, and it is advantageous to use the largest feasible scale for the desired application. Along these lines, the energy density scaling relationship defined by equation (58) makes it possible to extrapolate device performance to practical scales from the baseline laboratory scale experimental results. As an example, consider a pulse detonation MHD generator that is similar in all respects to the laboratory device with the exception of channel size and applied magnetic field. Choosing values consistent with practical implementation of this concept, a channel height and width of 20 cm, an active interaction length of 1 m, and an applied magnetic induction of 2.4 T was selected.

As a preliminary task to quantifying performance scaling with size, it is first necessary to estimate the magnitude of near-electrode potential losses in a practical device. Past experience with MHD devices, for instance, indicates that the near-electrode voltage drop can be reduced considerably below that encountered in the present device, which was operated only in single-shot mode and therefore suffered from severe cold wall effects. In principle, Δ can be reduced immensely by allowing the electrodes to operate at high temperature extremes. Based on past experience, being able to limit the voltage drop to no more than 10 percent of the induced field is anticipated. Holding the right-hand side of equation (58) constant, an energy density gain above the baseline experimental results in the following estimate:

$$\frac{\left(W_D/whL\right)_{\Delta=0.1}}{\left(W_D/whL\right)_{\Delta=0.6}} = \frac{(1-0.1)^2}{(1-0.6)^2} = 5.1 \quad . \tag{59}$$

For $v_0 = 50$ V (i.e., $B_{eff} = 2.4$ T), figure 24 yields $(W_D/whL)_{\Delta=0.6} \approx 300$ J/m^3 at optimal loading conditions. Correcting for the anticipated reduction in Δ using equation (59) results in $(W_D/whL)_{\Delta=0.1} = (5.1)(300) =$ 1,500 J/m^3 per detonation.

The performance gain associated with increased size follows from the multiplication of the corrected energy density with the active channel volume. That is, $(W_D)_{\Delta=0.1} = (whL)(W_D/whL)_{\Delta=0.1} =$ $(0.2)(0.2)(1)(1{,}500) = 60$ J per detonation. Assuming a practical repetition rate $f = 100$ cycles per second, a continuous power output of magnitude $P = f(W_D)_{\Delta=0.1} = (100)(60) = 6{,}000$ W_e is deduced.

Owing to the poor seeding characteristics of the present device, the preceding value represents a very conservative estimate of electrical power generation potential. For instance, the theoretical calculations shown in figure 20 indicate that electrical conductivity behind the detonation front can be increased as much as 5 times above the level measured in the device. This would imply a direct fivefold increase in electrical power generation performance. Optimization of seeding characteristics will require careful tailoring of injector configurations and atomization processes so that a uniform seed distribution is obtained along the channel length.

3.3.4 Thrust Characteristics

The dynamic load cell was also installed on the test stand and a series of shots were performed, with and without MHD interaction, to establish baseline thrust performance. Due to the low conductivity level experienced in these experiments, MHD interaction and enthalpy extraction were both very low, and the measured thrust profiles were found to be independent of MHD effects.

An ensemble-average profile of time-resolved engine thrust measurements is shown in figure 25. In general, the thrust-producing process may be broken into two phases: (I) A very short period of approximately constant thrust during which the detonation wave propagates from the closed end of the tube through the stationary mixture to the end of the chamber, and (II) a long period of exponentially decaying thrust associated with chamber blowdown.

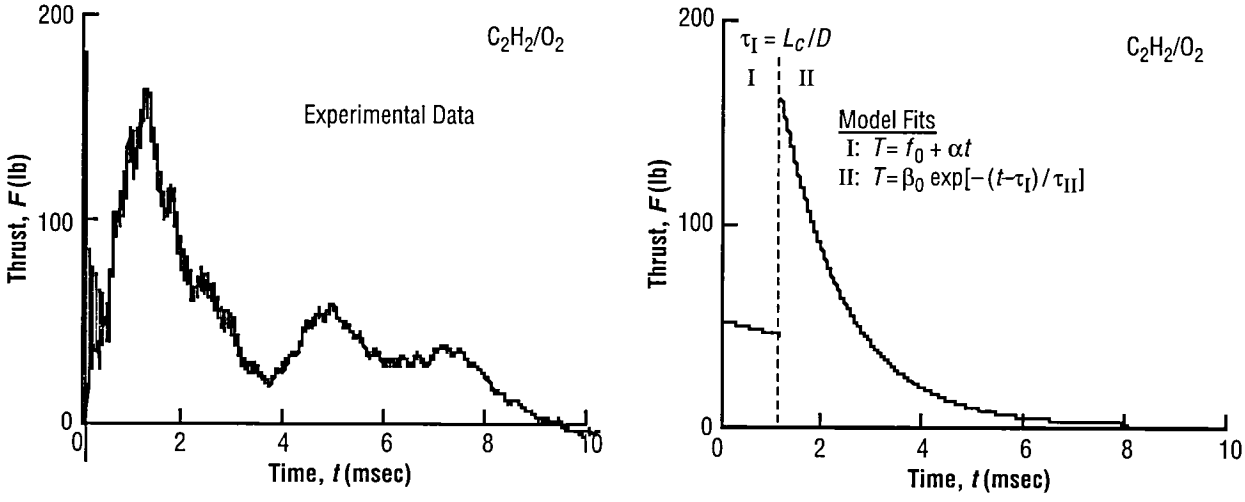

Figure 25. Ensemble-averaged thrust profile without MHD interaction and fitted model profile.

The timescale for phase I is readily determined from the ratio of the chamber length L_c to the detonation wave speed D ($\tau_I \approx L_c/D$). The thrust produced during this period is due solely to the pressure acting on the closed end of the tube since there is no chamber exhaust until the detonation wave exits the chamber. Due to the Taylor wave,[27] a centered expansion occurs between the detonation wave and the closed end of the tube, where the velocity must go to zero. Therefore, the pressure at the closed end can be expected to remain at an approximately constant low level as the detonation front proceeds through the chamber. The thrust is approximated during this phase by a linear relationship:

$$F_I = f_0 + \alpha t \quad , \tag{60}$$

where f_0 is a constant and α is the time rate of change in thrust.

The timescale for phase I depends upon the blastwave characteristics and the engine geometry. In general, it is reasonable to assume that the thrust during phase II may be approximated by an exponentially decaying function:

$$F_{\mathrm{II}} = \beta \exp\left[\frac{-(t-\tau_{\mathrm{I}})}{\tau_{\mathrm{II}}}\right] \quad , \tag{61}$$

where β is a constant and τ_{II} is the characteristic decay time for blowdown.

The model fits to the ensemble-averaged thrust profile are also shown in figure 25. It is interesting to estimate the average pressure at the closed end of the tube from the fitted value of $f_0 = 51$ lb. In this case,

$$p_{\mathrm{wall}} = \frac{f_0}{A_c} = \frac{51 \text{ lb}}{0.785 \text{ in.}^2} \approx 64 \text{ psi} \quad . \tag{62}$$

This implies a pressure ratio of only 4 with respect to the atmosphere. The actual average chamber pressure ratio is much higher of course when one averages over the entire centered expansion.

The I_{sp} for our apparatus was deduced from the ensemble-averaged thrust profile. This was done by first evaluating the total impulse of the system as

$$I = \int_0^{t_{\mathrm{cycle}}} F(t)\, dt = 0.43 \text{ lb} \cdot \text{sec} \quad . \tag{63}$$

The mass of propellant consumed per cycle m_p could be defined in terms of the scavenging ratio R_s

$$m_p = \int_0^{t_{\mathrm{cycle}}} \dot{m}(t)\, dt = V_c \rho_s R_s \quad . \tag{64}$$

Assuming $R_s = 1$, one deduces $m_p = 0.982$ g (2.16×10^{-3} lbm). The I_{sp} is then determined by

$$I_{sp} = \frac{I}{w_p} = \frac{I}{(g/g_c) m_p} \quad , \tag{65}$$

where w_p is the propellant weight, g is the Earth's gravitational acceleration, and g_c is a conversion factor. This yields an I_{sp} of 200 sec.

These thrust measurements alone are of great practical interest. Although the many potential advantages of PDE's have been duly noted, the open scientific literature contains no meaningful comparison with conventional aerospace propulsion systems, and much confusion exists with respect to representative performance parameters. Specific impulse estimates have generally been inferred from comparisons of

steady Brayton and Humphrey cycles, but these estimates do not take into account the unsteady nature of the blowdown process and the dramatic manner in which the real process differs from the idealized thermodynamic cycle.

In some cases, I_{sp} comparisons have been based on the pressure rise created by the detonation process, but this is not the pressure that provides thrust in the PDE cycle. The centered expansion that follows a detonation in a closed tube reduces the detonation pressure ratio from ≈18 for stoichiometric H_2/O_2 to an overpressure of ≈10, a value more representative of actual thrust performance. Measured I_{sp}'s for PDRE's have been reported in the range of 150 to 250 sec, but these have not been compared to conventional rocket engine performance at equivalent conditions. Furthermore, no I_{sp} estimates have included the effects of a nozzle.

From this viewpoint, it is useful to compare the thrust performance of the present pulse detonation apparatus with that of an equivalent conventional rocket engine. Equivalent conditions are defined as the same oxidizer-to-fuel ratio, the same nozzle type, and similar combustor pressure. Because the apparatus is based on a constant cross-sectional area with no divergent section, the conventional rocket performance should be computed based on a convergent nozzle only. Unfortunately, specification of chamber pressure is problematic due to the centered expansion process following the detonation wave. To provide perspective, a conventional rocket calculation was performed with the NASA SP–273 code using the C-J detonation pressure for C_2H_2/O_2 (33.6 atm) as the rocket chamber pressure. The computed I_{sp} of 120 sec for the nozzleless rocket may be compared with the measured value of 200 sec for the pulse detonation apparatus.

4. CONCLUSIONS

The prospects for realizing an integrated pulse detonation propulsion and MHD power system were examined. This included a critical evaluation of operational power requirements for direct detonation initiation of various fuel-oxidizer mixtures and the pumping power requirements for effective scavenging of the chamber. In addition, a series of experiments were conducted to investigate the basic engineering performance characteristics of a laboratory-scale, single-cycle pulse detonation-driven MHD generator. The experimental results reported here were only for stoichiometric mixtures of C_2H_2 and O_2 with an atomized spray of CsOH dissolved in alcohol as an ionization seed in the active MHD region. A plasma diagnostic channel was first attached to the detonation tube as a means of investigating ionization properties behind the detonation front. A continuous-electrode Faraday channel was subsequently attached to the detonation tube as a means of investigating MHD power generation characteristics. Time-resolved thrust characteristics of the single-cycle device were determined as well using a dynamic load cell incorporated into the thrust stand.

The critical energy requirements for direct detonation initiation of various fuel-oxidizer mixtures were deduced from available experimental data and theoretical models. The resulting data were critiqued and summarized in tabular form. Using an established model, analyses were made of the variation in critical energy with igniter deposition power for stoichiometric H_2/O_2 and H_2/air mixtures. In general, the use of practical fuel-oxidizer mixtures in high firing rate PDE's that may require a substantial amount of electrical power for direct detonation initiation was concluded. For H_2/O_2 mixtures, the critical energy for direct detonation initiation ranged from 0.1 to 1 J/cm^2, depending on the average deposition power; that is, the critical energy fell as the deposition power increased. The critical energy for H_2/air mixtures was more than an order of magnitude higher than the H_2/O_2 case.

The pumping power required for effective scavenging and recharging of the chamber was also addressed. This was accomplished through the introduction of a scavenging ratio parameter and a scavenging efficiency parameter. These parameters were then used to develop scaling relationships for the required scavenging pressure ratio in the engine as well as the pumping power needed to achieve the required scavenging pressure. Representative calculations based on these scaling relationships demonstrate that significant pumping power may be necessary for effective scavenging of practical engines.

In practice, this operational power must be obtained from either an independent, onboard power generation unit or from a power generator that is integrated into the engine. An independent power unit is feasible, but it negates the potential benefits of PDE's associated with reduced weight, simplicity, and cost. On the other hand, PDE's, unlike gas turbines, lack rotating shaft power to drive an integrated electrical generator of conventional design. If the electrical conductivity of the burned gas behind the detonation front is sufficiently high, however, it appears that an MHD generator may perform this function adequately.

The laboratory-scale experiments of this work yielded data on detonation wave ionization properties, MHD power extraction characteristics, and thrust performance. Useful scaling relationships were also developed which permit extrapolation of data from small-scale units to practical-sized devices.

Measurements using a short-length plasma diagnostic channel attached to the end of the detonation tube confirmed the attainment of detonation conditions ($p_2/p_1 \sim 34$ and $D \sim 2{,}400$ m/sec) and yielded detailed information with respect to ionization quality and gas-dynamic structure. For instance, the measured effective electrical conductivity of the burned ionized gas was $\sigma \sim 6$ S/m according to both two- and four-electrode probing techniques, and the measured dimensionless near-electrode voltage drop was $\Delta \sim 0.6$. The conductivity value was low relative to theoretical expectations and indicated that the seeding mechanism of this experiment was far from optimized. The magnitude of the dimensionless near-electrode voltage drop is characteristic of small-scale devices and can be minimized by increasing electrode temperature and increasing channel height. The delayed appearance ($\approx$1.5 msec behind the detonation front) of a secondary conductive wave that was most likely associated with flow reversal in the channel during the latter portion of the blowdown process was also observed. This effect is due to the single-cycle operational limit of the device in which the head end of the tube remains closed throughout the cycle. It is also worth noting that a receding Cher-Kistiakowsky secondary compression wave emerged in the acquired static pressure waveforms at a time delay of $\approx$400 μsec behind the detonation front.

Power extraction experiments were conducted using a short-length, continuous-electrode Faraday channel. The channel was placed in the bore of a magnet and attached to an active loading circuit in order to simulate higher effective magnetic induction. The following conclusions were reached with respect to power extraction: The measured peak open-circuit voltage was $V_{oc} = uBh \sim 10$ V, yielding an effective burned gas velocity of 660 m/sec; measured load line characteristics were linear away from the extreme loading conditions and indicated decreasing internal plasma resistance with increasing magnetic induction; the energy density scaling parameter ranged from 10 to 10^3 J/m^3 as the effective magnetic induction was varied from 0.6 to 4.2 T; optimal power extraction shifted from a load impedance of 10 Ω, when $v_0 = 0$ V, to 5 Ω, when $v_0 = 100$ V, due to decreasing internal plasma resistance as the effective magnetic induction and Joule dissipation increased; theoretical predictions for the energy density scaling parameter were in reasonable agreement with measurements, given the uncertainties in parameter values; and by scaling up to a practical-sized device and limiting the near-electrode potential drop to 10 percent of the induced Faraday potential, a fivefold to tenfold increase in power generation performance with respect to our laboratory-scale results is anticipated.

Time-resolved thrust measurements were also obtained and it was found that the thrust profile could be separated into two distinct phases. The first phase is characterized by a short-term, nearly constant thrust level while the detonation wave propagates through the chamber. The second phase is characterized by a decaying exponential-like thrust profile associated with chamber blowdown. The I_{sp} of the single-cycle device was determined to be $\approx$200 sec. Calculations for an equivalent nozzleless rocket yielded an I_{sp} of 120 sec.

REFERENCES

1. Bussing, T.; and Pappas, G.: "Pulse Detonation Engine Theory and Concepts," *Developments in High-Speed-Vehicle Propulsion Systems*, Progress in Astronautics and Aeronautics, AIAA, New York, S.N.B. Murthy and E.T. Curran (eds.), Vol. 165, pp. 421–472, 1997.

2. Lynch, E.D.; and Edelman, R.B.: "Analysis of the Pulse Detonation Wave Engine," *Developments in High-Speed-Vehicle Propulsion Systems*, Progress in Astronautics and Aeronautics, AIAA, New York, S.N.B. Murthy and E.T. Curran (eds.), Vol. 165, pp. 473–516, 1997.

3. Cambier, J.-L.; and Tegner, J.K.: "Strategies for Pulsed Detonation Engine Performance Optimization," *J. Propulsion and Power*, Vol. 14, No. 4, pp. 489–498, July–August 1998.

4. Jimerin, D.G.; Mironov, E.A.; and Popov, V.A.: "MHD Energy Conversion Using Detonation Conditions," *12th Symp. on Engineering Aspects of MHD*, Argonne National Laboratory, Argonne, IL, pp. II.4.1–II.4.7, 1972.

5. Lee, J.H.S.: "Initiation of Gaseous Detonations," *Ann. Rev. Phys. Chem.*, Vol. 28, pp. 75–104, 1977.

6. Zeldovich, Y.B.; Kogarko, S.M.; and Siminov, N.N.: "An Experimental Investigation of Spherical Detonation of Gases," *Sov. Phys. Tech. Phys.*, Vol. 1, Part 8, pp. 1689–1713, 1956.

7. Lee, J.H.S.: "Dynamic Parameters of Gaseous Detonations," *Ann. Rev. Fluid Mech.*, Vol. 16, pp. 311–336, 1984.

8. Benedick, W.B.; Guirao, C.M.; Knystautas, R.; and Lee, J.H.S.: "Critical Charge for the Direct Initiation of Detonation in Gaseous Fuel-Air Mixtures," *Dynamics of Explosions*, Progress in Aeronautics and Astronautics, J.R. Bowen, J.-C. Leyer, and R.I. Soloukhin (eds.), Vol. 106, pp. 181–202, 1986.

9. Lee, J.H.S.; and Matsui, H.: "A Comparison of the Critical Energies for Direct Initiation of Spherical Detonations in Acetylene-Oxygen Mixtures," *Combust. Flame*, Vol. 28, pp. 61–66, 1977.

10. Matsui, H.; and Lee, J.H.: "On the Measure of the Relative Detonation Hazards of Gaseous Fuel-Oxygen and Air Mixtures," *17th Symp. (Int.) on Combustion*, Combustion Institute, Pittsburgh, PA, pp. 1269–1280, 1978.

11. Beeson, H.D.; McClenagan, R.D.; Bishop, C.V.; and Benz, F.J.: "Detonability of Hydrocarbon Fuels in Air," *Dynamics of Detonations and Explosions: Detonations*, Progress in Aeronautics and Astronautics, A.L. Kuhl, J.-C. Leyer, A.A. Borisov, and W.A. Sirignano (eds.), Vol. 133, pp. 19–36, 1989.

12. Abouseif, G.E.; and Toong, T.Y.: "On Direct Initiation of Gaseous Detonations," *Combust. Flame*, Vol. 45, pp. 39–46, 1982.

13. Taylor, G.I.: "The Air Wave Surrounding an Expanding Sphere," *Proc. Roy. Soc. London, Ser. A*, Vol. 186, pp. 273–292, 1946.

14. Chu, B.T.: "Pressure Waves Generated by Addition of Heat in a Gaseous Medium," *NACA TN–3411*, 1955.

15. Erpenbeck, J.J.: "Stability of Idealized One-Reaction Detonations," *Phys. Fluids*, Vol. 7, No. 5, pp. 684–696, 1964.

16. Shepherd, J.E.: "Chemical Kinetics of Hydrogen-Air Diluent Detonations," *Dynamics of Explosions*, Progress in Aeronautics and Astronautics, J.R. Bowen, J.-C. Leyer, and R.I. Soloukhin (eds.), Vol. 106, pp. 263–293, 1986.

17. Moen, I.O.; Funk, J.W.; Ward, S.A.; Rude, G.M.; and Thibault, P.A.: "Detonation Length Scales for Fuel-Air Explosives," *Progress in Aeronautics and Astronautics*, Vol. 94, pp. 55–79, 1984.

18. Self, S.A.; and Kruger, C.H.: "Diagnostic Methods in Combustion MHD Flows," *J. Energy*, Vol. 1, No. 1, pp. 25–43, 1977.

19. Wu, Y.C.L.: "Performance Theory of Diagonal Conducting Wall MHD Generators," *AIAA J.*, Vol. 14, No. 10, pp. 1362–1368, 1976.

20. Gordon S.; and McBride, B.J.: "Computer Program for Calculation of Complex Chemical Equilibrium Compositions, Rocket Performance, Incident and Reflected Shocks, and Chapman-Jouguet Detonations," *NASA SP–273*, 1971.

21. Glassman, I.: *Combustion*, 2nd ed., Academic, Orlando, FL, p. 222, 1987.

22. Bityurin, V.A.: Private Communication, Institute of High Temperatures (IVTAN), Russian Academy of Sciences, Moscow, Russia, 1998.

23. Kistiakowsky, G.B.; and Mangelsdorf, P.C.: "Gaseous Detonations. VIII. Two-Stage Detonations in Acetylene-Oxygen Mixtures," *J. Chem. Phys.*, Vol. 25, No. 3, pp. 516–519, 1956.

24. Cher, M.; and Kistiakowsky, G.B.: "Gaseous Detonations. XI. Double Waves," *J. of Chem. Phys.*, Vol. 29, No. 3, pp. 506–511, 1958.

25. Basu, S.: "Ionization of Seeded Detonation Waves," *Phys. Fluids*, Vol. 3, No. 3, pp. 456–463, 1960.

26. Frost, L.S.: "Conductivity of Seeded Atmospheric Pressure Plasma," *J. Appl. Phys.*, Vol. 32, No. 10, pp. 2029–2039, 1961.

27. Taylor, G.I.: "The Dynamics of the Combustion Products Behind Plane and Spherical Detonation Fronts in Explosives," *Proc. Roy. Soc. London, Ser. A*, Vol. 200, pp. 235–247, 1950.

REPORT DOCUMENTATION PAGE

Form Approved
OMB No. 0704-0188

1. AGENCY USE ONLY *(Leave Blank)*	2. REPORT DATE	3. REPORT TYPE AND DATES COVERED
	January 2001	Technical Publication

4. TITLE AND SUBTITLE
Integrated Pulse Detonation Propulsion and Magnetohydrodynamic Power

5. FUNDING NUMBERS

6. AUTHORS
R.J. Litchford

7. PERFORMING ORGANIZATION NAMES(S) AND ADDRESS(ES)
George C. Marshall Space Flight Center
Marshall Space Flight Center, AL 35812

8. PERFORMING ORGANIZATION REPORT NUMBER
M–1002

9. SPONSORING/MONITORING AGENCY NAME(S) AND ADDRESS(ES)
National Aeronautics and Space Administration
Washington, DC 20546–0001

10. SPONSORING/MONITORING AGENCY REPORT NUMBER
NASA/TP—2001–210801

11. SUPPLEMENTARY NOTES
Prepared by the Advanced Space Transportation Program, Space Transportation Directorate

12a. DISTRIBUTION/AVAILABILITY STATEMENT
Unclassified-Unlimited
Subject Category 75
Standard Distribution

12b. DISTRIBUTION CODE

13. ABSTRACT *(Maximum 200 words)*

The prospects for realizing an integrated pulse detonation propulsion and magnetohydrodynamic (MHD) power system are examined. First, energy requirements for direct detonation initiation of various fuel-oxygen and fuel-air mixtures are deduced from available experimental data and theoretical models. Second, the pumping power requirements for effective chamber scavenging are examined through the introduction of a scavenging ratio parameter and a scavenging efficiency parameter. A series of laboratory experiments were carried out to investigate the basic engineering performance characteristics of a pulse detonation-driven MHD electric power generator. In these experiments, stoichiometric oxy-acetylene mixtures seeded with a cesium hydroxide/methanol spray were detonated at atmospheric pressure in a 1-m-long tube having an i.d. of 2.54 cm. Experiments with a plasma diagnostic channel attached to the end of the tube confirmed the attainment of detonation conditions ($p_2/p_1 \sim 34$ and $D \sim 2{,}400$ m/sec) and enabled the direct measurement of current density and electrical conductivity (≈6 S/m) behind the detonation wave front. In a second set of experiments, a 30-cm-long continuous electrode Faraday channel, having a height of 2.54 cm and a width of 2 cm, was attached to the end of the tube using an area transition duct. The Faraday channel was inserted in applied magnetic fields of 0.6 and 0.95 T, and the electrodes were connected to an active loading circuit to characterize power extraction dependence on load impedance while also simulating higher effective magnetic induction. The experiments indicated peak power extraction at a load impedance between 5 and 10 Ω. The measured power density was in reasonable agreement with a simple electrodynamic model incorporating a correction for near-electrode potential losses. The time-resolved thrust characteristics of the system were also measured, and it was found that the MHD interaction exerted a negligible influence on system thrust and that the measured I_{sp} of the system (200 sec) exceeded that computed for an equivalent nozzleless rocket (120 sec).

14. SUBJECT TERMS	15. NUMBER OF PAGES
pulse detonation engine, combustion, magnetohydrodynamics, propulsion, power	56
	16. PRICE CODE A04

17. SECURITY CLASSIFICATION OF REPORT	18. SECURITY CLASSIFICATION OF THIS PAGE	19. SECURITY CLASSIFICATION OF ABSTRACT	20. LIMITATION OF ABSTRACT
Unclassified	Unclassified	Unclassified	Unlimited

National Aeronautics and
Space Administration
AD33
George C. Marshall Space Flight Center
Marshall Space Flight Center, Alabama
35812